Available online at www.sciencedirect.com

ScienceDirect

Geochimica et Cosmochimica Acta 305 (2021) 263–281

Geochimica et Cosmochimica Acta

www.elsevier.com/locate/gca

H diffusion in orthopyroxene and the retention of mantle water signatures

Alexandra Demers-Roberge [a,*], Michael C. Jollands [a,b], Peter Tollan [c,d], Othmar Müntener [a]

[a] *Institut des sciences de la Terre, Université de Lausanne, 1015 Lausanne, Switzerland*
[b] *Lamont-Doherty Earth Observatory, Columbia University, 61 9W Road, Palisades, NY 10964, United States*
[c] *Institut für Geologie, Universität Bern, Baltzerstrasse 1+3, 3012 Bern, Switzerland*
[d] *Institute of Geochemistry and Petrology, Universität Zürich, Clausiusstrasse 25, 8092 Zürich, Switzerland*

Received 14 July 2020; accepted in revised form 1 April 2021; Available online 16 April 2021

Abstract

Natural gem quality orthopyroxene crystals were experimentally dehydrated between 720 °C and 1020 °C, varying silica activity (buffered by olivine-orthopyroxene or orthopyroxene-quartz), oxygen fugacity (log f_{O2} relative to the quartz-fayalite-magnetite buffer (QFM) of around +1, −1 and −7) and composition (two different orthopyroxene types) to study these parameters' effects on both the diffusivity of hydrogen and the Fourier transform infrared (FTIR) spectra in orthopyroxene. Hydroxyl profiles were measured across partially dehydrated grains, from which H diffusion coefficients were extracted. Fitting these H diffusion coefficients to the isobaric Arrhenius relationship, $\log D = \log D_0 - E_a/(2.303RT)$, gives $\log D_0$ of −5.11, −4.93 and −5.52 m^2/s, and E_a of 139, 149 and 125 kJ mol^{-1} for the [100], [010] and [001] axes, respectively, where D_0 is the pre-exponential factor (m^2/s), E_a is the activation energy (kJ mol^{-1}), R is the universal gas constant (kJ mol^{-1} K^{-1}) and T is the temperature (K). Hydrogen diffusivities at ~ΔQFM-1 and 700 °C to 1000 °C are between $\log D = -12.5$ to −10.4 m^2/s. This is similar to the fastest H diffusivity measured in olivine, suggesting diffusion primarily by a 'proton-polaron'-type mechanism, whereby the movement of protons through the crystal is associated with Fe redox, with the net result being that dehydration should be accompanied by Fe oxidation. The determined diffusion coefficients are ~0.3 log units faster than those determined in H-^{2}H self-diffusion experiments (Stalder and Behrens, 2006). The effect of a_{SiO2} and f_{O2} (between ~ΔQFM-1 to ~ΔQFM + 1) is only minor or within uncertainty. These data were applied to a natural sample from a xenolith from Las Cumbres in Chilean Patagonia, where orthopyroxene shows > 500 μm H loss profiles in length, and olivine shows 50–200 μm Fe-Mg, Y, Ti, V and Sc profiles on millimeter sized crystals. Modelled timescales calculated from a H profile in orthopyroxene, using our H diffusivities along with published values, are considerably shorter (minutes to days) compared to those derived from Fe-Mg inter-diffusion in olivine (weeks to years) from the same xenolith using Fe-Mg diffusivities in olivine. This discrepancy is likely due to H-loss in the natural orthopyroxene representing the timescale between the onset degassing of the host magma and emplacement, whereas Fe-Mg inter-diffusion records the time elapsed

* Corresponding author.
E-mail address: alexandra.demers-roberge@unil.ch (A. Demers-Roberge).

https://doi.org/10.1016/j.gca.2021.04.005

between xenolith entrainment and final emplacement. This supports previous assertions that H diffusion in orthopyroxene is sufficiently fast such that many xenolith-hosted orthopyroxene crystals may have suffered significant re-equilibration with the host magma H_2O prior to later degassing-induced H-loss.

Keywords: Hydrogen diffusion; Hydrogen in orthopyroxene; Nominally Anhydrous Minerals; Time of ascent of xenoliths; Experimental constraints on H diffusion in orthopyroxene; Gem-quality natural enstatite hydrogen diffusivities; Reliability of water contents recorded by orthopyroxene; H-loss profiles in mantle orthopyroxene

1. INTRODUCTION

Olivine (ol), clinopyroxene (cpx) and orthopyroxene (opx), which comprise the majority of the Earth's uppermost mantle, are nominally anhydrous but contain 'water' as a trace component (generally < 0.1 wt. %). In these nominally anhydrous minerals (NAMs) 'water' generally refers to H incorporated in the crystal lattice and bonded to structural oxygen. The presence of small amounts of water in NAMs can dramatically modify various physical properties of Earth's upper mantle, including solidi and liquidi (Sarafian et al., 2017), rheology (Mackwell et al., 1985; Karato and Jung, 2003; Kohlstedt, 2006), viscosity (Hirth and Kohlstedt, 1996), mechanical strength (Kavner, 2003), electrical conductivity (Karato, 1990; Schlechter et al., 2012; Selway et al., 2014), seismic wave attenuation (Aizawa et al., 2008) and deformation patterns (Jung et al., 2006; Manthilake et al., 2013). Xenolith-hosted NAMs contain highly variable amounts of H_2O, reflecting the characteristics of the surrounding mantle environment (pressure, temperature, chemical composition, water fugacity, oxidation state), the composition of the crystal, as well as the nature of the entraining melt and the rate of ascent (e.g. Peslier, 2010; Demouchy and Bolfan-Casanova, 2016; Peslier et al., 2017).

Since the 1970 s, it was recognized that pyroxenes could include small amounts of OH, independently from the presence of amphibole lamellae (Wilkins and Sabine, 1973; Beran, 1976; Ingrin et al., 1989). The water content of orthopyroxene (30–400 wt. ppm H_2O) (Ingrin and Skogby, 2000; Demouchy and Bolfan-Casanova, 2016) as well as its abundance (Frey and Prinz, 1978) means that for typical upper mantle compositions, it may store the majority of hydrogen. Though hydrogen contents are often measured in orthopyroxene from mantle xenoliths, the relevant incorporation and diffusion mechanisms are still not fully understood. Measurements of natural mantle orthopyroxene have frequently suggested that it is a relatively reliable (compared to olivine) host of water, based on the absence of H diffusion profiles in samples which displayed clear evidence of H-loss in coexisting olivine (Gose et al., 2009; Peslier, 2010; Xia et al., 2010; Warren and Hauri, 2014; Demouchy and Bolfan-Casanova, 2016; Xia et al., 2019). This suggestion has been challenged in more recent studies of natural mantle orthopyroxene (Tian et al., 2017; Denis et al., 2018; Tollan and Hermann, 2019; Xu et al., 2019; Wang et al., 2021) which have found strong evidence for rapid diffusion of H, broadly supporting inferences from experiments (Stalder and Skogby, 2003; Stalder and Behrens, 2006). The specific conditions that govern the reliability of orthopyroxene as a recorder of mantle H remain unclear, thus warrant further research.

In pure synthetic enstatite, where the only available substitution mechanisms should be $Si^{4+} = 4H^+$ and $Mg^{2+} = 2H^+$, the H solubility is moderate and pressure-dependent (Rauch and Keppler, 2002). In general, the H solubility in orthopyroxene increases with the addition of trivalent cations, generically R^{3+} (Al^{3+}, Fe^{3+} or Cr^{3+}; Rauch and Keppler, 2002; Stalder, 2004), allowing $2\ Mg^{2+} = R^{3+} + H^+$ and $Si^{4+} = R^{3+} + H^+$ substitutions. However, this general relationship is complicated by the formation of Tschermak-type defects (Kohn et al., 2005; Stalder et al., 2005; Prechtel and Stalder, 2012; Stalder et al., 2015). Hydrogen diffusivities in orthopyroxene depend to some extent on the relevant incorporation mechanism. The $Mg^{2+} = 2H^+$ mechanism shows relatively low diffusivities, rate-limited by metal-vacancy diffusion (Stalder and Skogby, 2003). The $Al^{3+}+H^+$ and $Cr^{3+}+H^+$ substitutions are associated with relatively low H diffusivities (Stalder et al. 2005; Stalder and Behrens, 2006; Schlechter, 2011). Conversely, the presence of Fe enhances the diffusivity of H, up to a threshold value of Fe# (Fe/(Fe + Mg) ≥ 0.10 where diffusion becomes rate-limited by hydrogen self-diffusion (Stalder et al., 2007), which is significantly faster than hydrogen diffusivities associated with other diffusion mechanisms (Stalder and Behrens, 2006). Experiments using synthetic crystals have shown the complex interplays of vacancy diffusion (Stalder and Skogby, 2003), redox reactions (Stalder and Skogby, 2007; Stalder et al., 2007) and orientation dependent hydrogen self-diffusion (Stalder and Behrens, 2006) on hydrogen diffusivities in natural mantle orthopyroxene.

Although previous studies have shown that oxygen fugacity (f_{O2}) and silica activity (a_{SiO2}) have an important control on H incorporation (e.g. Sundvall and Skogby, 2011; Prechtel and Stalder, 2012; Tollan and Hermann, 2019), the influence of these parameters on H diffusion is not well constrained. Some features of the orthopyroxene infrared spectra also remain unexplained. For example, the 3570 cm^{-1} peak in FTIR spectra, which is one of the main contributor to the absorbance of natural mantle orthopyroxene, has no defect assignation experimental studies using synthetic systems.

To address some of these remaining issues, a series of orthopyroxene dehydration experiments were conducted at 1 bar between 720 °C and 1020 °C, at f_{O2} varying between ~ΔQFM + 1, ~ΔQFM-1 and ~ΔQFM-7, and with a_{SiO2} buffered by ol-opx and opx-SiO_2. These complement

the existing data with a new set of hydrogen diffusion coefficients, which considers the effects of f_{O2}, a_{SiO2}, temperature, chemical composition on hydrogen diffusion and incorporation mechanisms. We then use these new diffusion data, as well as existing data, to calculate ascent timescales from H profiles in natural orthopyroxene from a mantle xenolith from Chilean Patagonia.

2. METHODS

2.1. Experimental methods

2.1.1. Characterisation of the starting material

When designing diffusion experiments in crystals, it is generally necessary to choose between two classes of starting materials. Firstly, there are the crystals with compositions that are directly relevant to the natural setting being considered, but are often (1) unavailable in large quantities, (2) heterogeneous and/or (3) small/imperfect (i.e. fractured). Secondly, there are the gem quality/synthetic crystals, which are generally more homogenous and available in greater quantities and thus easier to work with, but may have compositions that are not directly applicable for the geological applications being considered. However, the extent to which a gem quality/synthetic crystal is applicable for other geological settings is generally not known at the beginning of an experimental campaign. In this study, we choose the second type of starting material, which may limit to some extent the applicability of our results to natural settings – this is discussed further below.

Most experiments were conducted using light brown, gem-quality, inclusion-free enstatite from Tanzania. Whilst the exact provenance of the crystal is not known, gemstones deposits in Tanzania are located in the Proterozoic, granulite facies Ubendian and Usagarans areas, which are parts of the Mozambique Belt of East Africa, (Malisa and Muhongo, 1990). The Kilosa-Mpwapwa region, where it is suspected to be from, is also a gold-bearing copper deposit area of skarn hydrothermal-epithermal origins (Sezerer-Kuru and Vural, 2015). The second starting material, used for some additional experiments, is a green inclusion-free gem-quality enstatite crystal of unknown provenance. The starting materials were initially ~5–7 mm and were generally cut into cuboids (~2 × 2 × 2 mm) with faces perpendicular to the principal crystallographic axes, except for some crystals which were cut parallel to (210), i.e. the main cleavage plane.

Major and minor elements (Si, Al, Cr, Ti, Fe Mg, Ni, Mn, Na, Ca, K) of both starting materials were measured by electron probe micro-analysis (EPMA), using a JEOL JXA-8530F hyperprobe operating at 15 kV and 15 nA (University of Lausanne). The following calibration standards were used: Si - wollastonite, Ti – rutile, Cr – chromite, Al – andalusite, Fe – fayalite, Mn – tephrite, Ni – NiO, Mg – forsterite, Ca – wollastonite, Na – albite and K – orthoclase. Trace elements (Cu, Zn, Rb, Sr, Y, Zr, Nb, Cs, Ba, REEs, Hf, Ta, Pb, Th, U) were measured by laser ablation inductively coupled plasma mass spectrometry (LA-ICP-MS), using a Thermo Element XR sector field mass spectrometer coupled to an Australian Scientific Instruments RESOlution 193 nm ArF excimer laser ablation system, equipped with a Laurin Technic S155 two-volume ablation cell, via He-Ar carrier gas (University of Lausanne). Analyses were conducted using a 100 μm diameter circular beam, ablating at 10 Hz and 6 J/cm^2. All analyses included 30 s of ablation and 60 s of background. The NIST SRM-612 glass was used as standard (values from Jochum et al., 2011).

Both starting materials are homogeneous in terms of major elements, with Mg# ($Mg^{2+}/(Mg^{2+}+Fe^{2+})$) of ~0.92 and ~0.93, ~0.11 and 0.39 wt.% Al_2O_3 and 0.02 and 0.19 wt.% Cr_2O_3 for the Tanzanian and green enstatite, respectively. Full major and trace elements analyses are presented in Appendix 1 (Tables A1 and A2). The Tanzanian orthopyroxene has low concentrations of most trace elements, with Rb, Ba, Th, U, Nb and Ta being below the detection limits of our LA-ICP-MS routine (Appendix 2 – Fig. B1).

To consider orientations, a ~centimetre size slab of Tanzanian orthopyroxene was cut parallel to (001), and polished using diamond grit (as described above), followed by colloidal silica polishing on a vibrating lap. An Oxford Instruments Tescan Mira II LMU (University of Lausanne), with a Nordlys S camera, was used for electron backscatter diffraction (EBSD) to verify the orientation of the cut plane and to determine the positions of the [100] and [010] vectors (Appendix 2 – Fig. B3). Kikuchi patterns were indexed using inbuilt Aztec 2.4 software. Then, two other crystals were cut parallel to (100) and (010).

2.1.2. Experimental methods

A total of 42 hydrogen diffusion experiments were conducted at varying temperature, silica activity (a_{SiO2}), oxygen fugacity (f_{O2}) and crystal orientation. a_{SiO2} was buffered using either opx-ol (ground San Carlos olivine and the same Tanzanian orthopyroxene as used for the experiments) or opx-SiO_2 (ground Tanzanian orthopyroxene with SiO_2 (α-quartz from Sigma-Aldrich)). The crystals were packed into one of the buffering powders in gold tubing (3 mm diameter), crimped on one end and open at the other. They were attached to an alumina ring with Pt wire, suspended from an alumina rod and inserted into a Gero 1-atm gas mixing vertical tube furnace at University of Lausanne. The f_{O2} (~ΔQFM + 1, −1, −7) was controlled using H_2–CO_2 mixes in appropriate proportions. Temperature (between 723 °C and 1020 °C) and was measured and controlled using Pt-Rh thermocouples (B-type). The experiments were ended by lifting the charges out of the furnace, upon which they were air-cooled. Following dehydration experiments, the crystals recovered were mounted in epoxy. For FTIR analyses, mounts were equally polished on both sides, down to a thickness of 300–500 μm, such that the measured section would be approximately the core of the crystals. The runs and the parameters are detailed in Table 1 and Table 2. All data regarding the experiments and their orientation can be found in the Supplementary data (S1-S3).

Table 1
Experimental runs and parameters at ~ΔQFM + 1 for the Tanzanian orthopyroxene.

Opx type *	T (°C)	Duration (min)	log f_{O2} (bars)	Δlog QFM	a_{SiO2} buffer	log D (m^2/s) ** Unoriented
TO, ~ΔQFM + 1	720	980	−15.2	+1.0	ol-opx	−12.46 (0.08§
						−12.40 0.09)§
	720	980	−15.2	+1.0	SiO_2 –opx	−12.29 (0.06)
						−12.14 (0.04)
	820	75	−12.8	+1.2	ol-opx	−11.39 (0.10)
						−11.29 (0.09)
	820	30	−12.8	+1.2	SiO_2 -opx	−11.11 (0.10)
						−11.23 (0.12)
		75				−11.71 (0.09)
	920	20	−11.2	+1.1	ol-opx	−10.93 (0.07)
						−11.08 (0.07)
		40				−10.89 (0.08)
	920	20	−11.2	+1.1	SiO_2 -opx	−10.88 (0.05)
						−11.10 (0.06)
		40				−11.08 (0.04)
						−11.14 (0.05)
	1020	10	−9.4	+1.1	ol-opx	−10.78 (0.05)
		20				−10.66 (0.09)
						−10.65 (0.05)
	1020	10	−9.4	+1.1	SiO_2 -opx	−10.87 (0.08
		20				−10.30 (0.06)§
						−10.04 (0.73)§

* TO: Tanzanian opx.
** σ is the uncertainty associated with the fit to Eq. (1) (1 standard deviation).
§ Log D calculated with a numerical solution of Eq. (1).

2.2. Analytical methods

2.2.1. Fourier-transform infrared (FTIR) spectroscopy

FTIR spectra were obtained at the University of Bern using a Bruker Tensor 27 infrared spectrometer, with a liquid nitrogen-cooled mercury cadmium telluride (MCT) detector coupled to a Bruker Hyperion infrared microscope, equipped with a continuously dry-air-purged plexiglass measurement chamber. All spectra were recorded between 500 cm^{-1} and 4000 cm^{-1} with 64 scans and 4 cm^{-1} resolution, then atmosphere and baseline-corrected using a concave rubberband tool with 64 baseline points, and 3 iterations, built into Bruker OPUS software. This method is described by Pirzer and Sawatzki (2008). This method tends to remove broad bands, thus may lead to an underestimation of total water content, but does not appreciably affect the areas of the sharp OH peaks. Diffusion coefficients determined using spectra corrected with a simple linear baseline, and those determined from spectra corrected using the rubberband, are the same within error (Appendix 2 – Fig. B4). Raw spectra are available in the Supplementary Material. FTIR spectroscopy had three purposes in this study: (1) to characterize the H_2O content of the Tanzanian orthopyroxene and the green enstatite prior to experiments; (2) to determine the orientation of diffusion relative to the principle axes in the crystals and (3) to measure H diffusion profiles following experiments. FTIR spectra were also collected from some natural samples. These are described in further detail in Section 4.2.

For (1), the mounts were doubly polished down to 400 μm with thicknesses measured at the cores of individual crystal using a digital micrometer. Unpolarized and polarized spectra were recorded with an on-sample aperture of 100 μm × 100 μm. For (2), the mounts with EBSD-oriented crystals were doubly polished, as above. Polarized spectra with E//[100], E//[010] and E//[001] were recorded on each of the three crystals (Fig. 1A). For (3), FTIR spectroscopy was used to measure hydrogen profiles across experimentally dehydrated crystals. Two perpendicular profiles (unpolarised) were recorded per crystal, with a 20 μm × 100 μm on-sample aperture and 20 μm point spacing. Polarized spectra were also recorded with the electric vector of the polarizer parallel to the measured profile direction. The absorbance in the Si-O region was then compared to reference spectra for E//[001], E//[010], E//[100] and E//[210] (Appendix 2 – Fig. B5) to determine/confirm the direction of diffusion.

After the measurements, the absorbance of the sample in the silica overtone (Si-O) (1500–2230 cm^{-1}) and the O-H stretching regions (3000–3700 cm^{-1}) were numerically integrated. The average of the integrated area of the Si-O overtone region over the profile was used to normalize to a constant thickness, and then the core thickness, measured with a digital micrometer, was used to normalize to 1 cm. Spectra were resolved into a series of Gaussian peaks using a MATLAB-based fitting routine. For the purposes of hydrogen diffusion modelling, at least in situations where diffusion can be assumed to be concentration-independent, it is generally not necessary to convert absorbance (Abs) into a H_2O content. However, where necessary, the H_2O concentration was determined using $0.067 \times \sum Abs_{1cm}$, where 0.067 is the absorption coefficient from Bell

Table 2
Experimental runs and parameters at ~ΔQFM-1 and ~ΔQFM-7 for the Tanzanian orthopyroxene and ~ΔQFM-1 for the green enstatite.

Opx type*	T (°C)	Duration (min)	Log f_{O2}	QFM	$a_{[SiO2]}$ buffer	log D **			
						[001]	[010]	[100]	Unoriented or [210]
TO, ~ΔQFM-1	723	915	−17.3	−1.1	ol-opx		−12.5^48 (0.08)		
	723	915	−17.3	−1.1	SiO_2 -opx	−12.21 (0.08)			−12.23 (0.07)
	769	265	−16.7	−0.9	ol-opx				−11.63 (0.06)
	769	265	−16.7	−0.9	SiO_2 -opx	−11.57 (0.10)§	−10.97 (0.39)§		
	826	60	−14.9	−1.2	ol-opx		−10.81 (0.32)	−11.72 (0.08)	
		180					−12.15 (0.10)	−11.77 (0.04)	
	826	30	−14.9	−1.2	SiO_2 -opx	−11.69 (0.24)		−12.43 (0.49)	
	875	60	−13.9	−1.0	ol-opx		−11.91 (0.12)	−11.22 (0.04)	
		320					−11.89 (0.05)	−11.56 (0.04)§	
	865	30	−14,3	−1.2	SiO_2 -opx	−11.03 (0.10)			
	875	60				−11.07 (0.06)			−11.61 (0.95)
	914	20	−13,4	−1.2	ol-opx	−11.05 (0.08)			−10.97 (0.08)
	914	20	−13,4	−1.2	SiO_2 -opx	−11.18 (0.11)			−11.62 (0.14)
	920	15	−13,1	−1.0	ol-opx	−10.98 (0.02)	−9.74 (0.05)§		
	975	15	−12,1	−0.8	ol-opx		−10.93 (0.09)		
		30				−10.60 (0.07)			−10.83 (0.08)
	975	15	−12,1	−0.8	SiO_2 -opx		−10.67 (0.11)	−11.17 (0.21)§	
		30					−11.17 (0.16)	−11.05 (0.15)	
	1013	10	−11,5	−0.7	ol-opx	−10.48 (0.08)		−10.80 (0.07)	
		20				−11.08 (0.07)		−10.56 (0.05)	
	1013	10	−11,5	−0.7	SiO_2 -opx	−10.41 (0.06)§		−10.93 (0.08)	
		20					−11.09 (0.15)	−11.05 (0.08)	
TO, ~ΔQFM-7	875	1280	−19.8	−6.8	ol-opx	−12.80 to −13.26			−12.88
	875	1280	−19.8	−6.8	SiO_2 -opx		-	-	
	960	495	−18.1	−6.7	ol-opx				−11.92
GE, ~ΔQFM-1	824	15	−14.9	−1.2	ol-opx		−10.83 (0.17)	−11.07 (0.22)	
		30					−11.82 (0.11)	−11.43 (0.14)	
		60				-		−10.76 (0.21)	

* TO: Tanzanian opx, GE: green enstatite.
** σ is uncertainty associated with the fit to Eq. (1) (1 standard deviation).
§ Log D calculated with a numerical solution of Eq. (1).

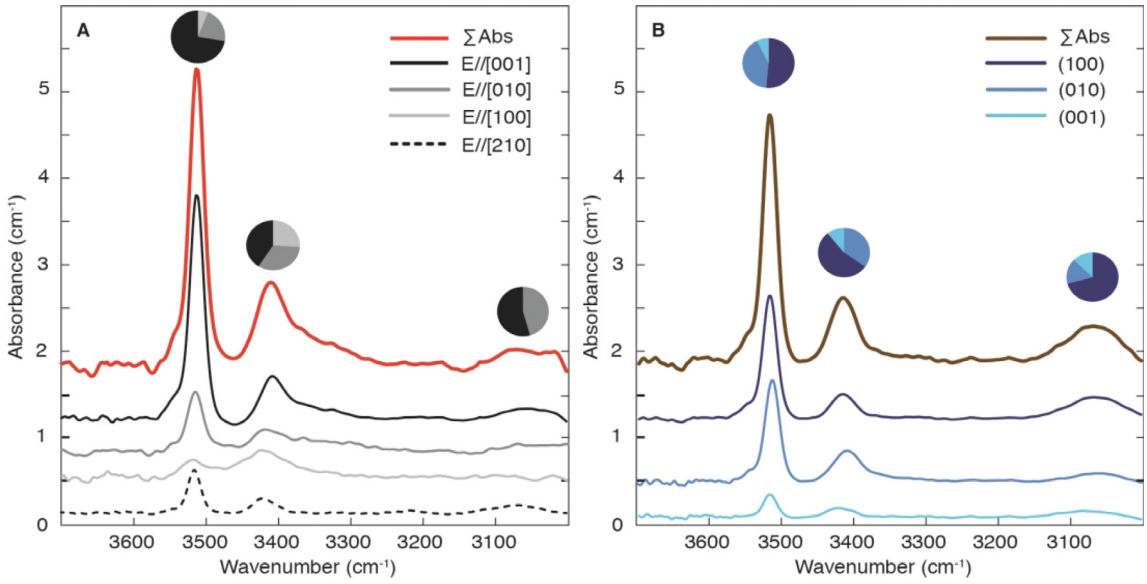

Fig. 1. Stacked FTIR spectra of the O-H bonding region (3000–3700 cm^{-1}) of the Tanzanian opx starting material. A) Polarized light: The three main crystallographic orientations, and the [210] direction are shown. The red line represents the sum of the spectra of E//[100], E//[010] and E//[001]. Pie charts show their contribution to the height of the bands. B) Unpolarized light measurement on the three main planes (100), (010) and (001). The brown line is the sum of the three spectra and the pie charts represent their contribution to the sum of the spectra. There is a 19% difference between the $\sum$Abs ($Abs_{E//[100]} + Abs_{E//[100]} + Abs_{E//[100]}$) with polarized light (A) and $\sum$Abs ($Abs_{(100)}$+$Abs_{(010)} + Abs_{(001)}$) with unpolarized light (B). The FTIR spectra related to panel A and B is available in Supplementary data – S4.

et al. (1995) and $\sum Abs_{1cm}$ is the total measured absorbance normalized to 1 cm. The total absorbance $\sum Abs_{1cm}$ is often approximated using $\sum Abs_{1cm} = Abs_{1cm} \times 3$ where Abs_{1cm} is the absorbance measured in a single plane normalized to 1 cm, and the coefficient 3 is an approximation accounting for the use of unpolarized light (Kovács et al., 2008; Sambridge et al., 2008; Jackson et al., 2018). This is only strictly appropriate either when (1) the absorbance represents an average of randomly oriented crystals (Kovács et al., 2008), or (2) absorbance is isotropic, such as in glass or cubic minerals, so the values should be treated as approximate only. This caveat is in addition to that associated with the potential removal of broad peaks associated with the concave rubber band baseline correction routine.

2.2.2. Characterization of mantle orthopyroxene

The natural orthopyroxene used in Section 4.2 was picked from orthopyroxene separates from peridotite sample EC_11, from Las Cumbres, Sierra Baguales, Chile. This locality is in Southern Patagonia, in the back-arc region associated with the subduction of the Nazca and the Antarctic plates below the South American plate. The crystal (plane view dimension: ~2 × 2.3 mm) was mounted in epoxy and doubly polished in the same way as the crystals used for the diffusion experiments. The exposed section has faces approximately parallel to (100). A liquid nitrogen-cooled focal plane array (FPA) detector was used to map the OH content of the crystal, using an aperture of 100 μm by 100 μm, 8 cm^{-1} resolution, 128 scans and a 2 × 2 binning. All spectra were recorded between 500 cm^{-1} and 4000 cm^{-1}. A profile across the core of the crystal was extracted from the FPA map. Additional WDS-EPMA maps of Fe, Cr, Al, Ca, Si, Mg were acquired from the crystal (15 kV, 4 nA, 10 ms dwell time). Backscattered electron images of the interface between the host basalt and olivine crystals of a thin section of sample EC_11 were taken. From these images, quantitative EPMA values of Mg and Fe were indexed to the grey scale image and Mg-Fe profiles were extracted. At the same location as the Fe-Mg profiles, continuous line scan profiles of Ti, V, Sc and Y, recorded using LA-ICP-MS, with a 10 × 100 μm slit, an energy of 8 mJ and at a speed of 1 μm/s, were acquired on the thin sections of the sample EC_11.

2.2.3. Diffusion modelling

Profiles of concentration versus distance were fitted to either analytical solutions or an explicit finite difference numerical approximation of Fick's second law (Eq. (1)) (Crank, 1979).

$$\frac{\partial C}{\partial t} = D\left(\frac{\partial^2 C}{\partial x^2}\right) \quad (1)$$

In most cases, and in line with other H diffusion studies (Stalder and Skogby, 2003; Carpenter, 2003; Stalder and Behrens, 2006; Stalder et al., 2007), diffusion was assumed to be concentration-independent, one dimensional, with constant boundary conditions. Four different shapes of concentration versus distance profiles were measured (Appendix 2 - Fig. B2): (1) half profiles with a plateau at the core (Eq. (2)) (Crank, 1979); (2) full profiles with a plateau at the core (Eq. (3)) (Carslaw and Jaeger, 1959); (3) no plateau at the core (numerical solution to Eq. (1)) and (4) M-shaped profiles.

$$C = C_{core} + (C_{core} - C_{rim1}) \times \mathrm{erfc}\left(\frac{x}{2\sqrt{Dt}}\right) \quad (2)$$

$$C = C_{core} + (C_{core} - C_{rim1}) \times \mathrm{erfc}\left(\frac{x}{2\sqrt{Dt}}\right) + (C_{core} - C_{rim1}) \times \mathrm{erfc}\left(\frac{x_{max} - x}{2\sqrt{Dt}}\right) \quad (3)$$

In all equations, C_{core} is the core concentration (wt. ppm H_2O, proportional to absorbance), C_{rim1} and C_{rim2} are rim concentrations (wt. ppm H_2O, some fits required slightly different rim concentrations at the two edges), D is the diffusion coefficient, assuming concentration-independence (m^2/s), t is time (s), x and x_{max} as the position on the profile and the total length of the profile (m), respectively. The D calculated from the experiments is equivalent to $\tilde{D}$ of Kohlstedt and Mackwell (1998), which is the diffusivity measured in experiments by fitting diffusion profiles directly. To avoid making assumptions about the physical processes responsible for the M-shaped profiles, which could be due to H enrichment then depletion at the interface, or some interplay between diffusion and inter-site reaction (Jollands et al., 2019), diffusion coefficients were estimated using an approximation based on an estimated diffusion length (L), $L = 4\sqrt{Dt}$. L was estimated on some profiles (Fig. 4F) at the point at which the absorbance increases or decreases beyond the scatter associated with the core plateau.

3. RESULTS

3.1. FTIR spectra of the starting materials

To describe FTIR spectra, the terms peak and absorption bands will be used to refer to resolved peaks (as in Fig. 2) and non-resolved peaks (as a higher absorbance), respectively. In the OH stretching region of orthopyroxene, thickness-normalized absorbance (Abs) of individual bands are orientation dependent, with, in general, $Abs_{E//[001]} > Abs_{E//[010]} > Abs_{E//[210]} > Abs_{E//[100]}$. For the Tanzanian opx, the $\sum Abs \approx 138\ cm^{-2} \approx 9$ wt. ppm H_2O based on polarized measurements - this is low compared to mantle orthopyroxene (Demouchy and Bolfan-Casanova, 2016), again potentially due to the baseline correction, but this is not consequential for determination of diffusion coefficients (Appendix 2 – Fig. B4 D). $Abs_{E//[210]}$ is also shown since many crystals were cut with one plane parallel to (210). The main band groups in the Tanzanian orthopyroxene starting material spectra are 3000–3100 cm^{-1}, 3300–3450 cm^{-1} and 3475–3565 cm^{-1} (Fig. 1), with all bands showing strongest absorbance when E//[001].

3.2. Post-experiment core FTIR spectra

Post-experiment spectra extracted from crystal cores are consistently different to the spectra of the starting material. All the core spectra presented and described in this section are "true" cores as they were extracted from the center of profiles showing a flat plateau at the core of the crystals. The core spectra are affected, to varying degrees, by the experimental a_{SiO2}, f_{O2}, temperature and time. The following describes these effects, with spectra available in Supplementary data.

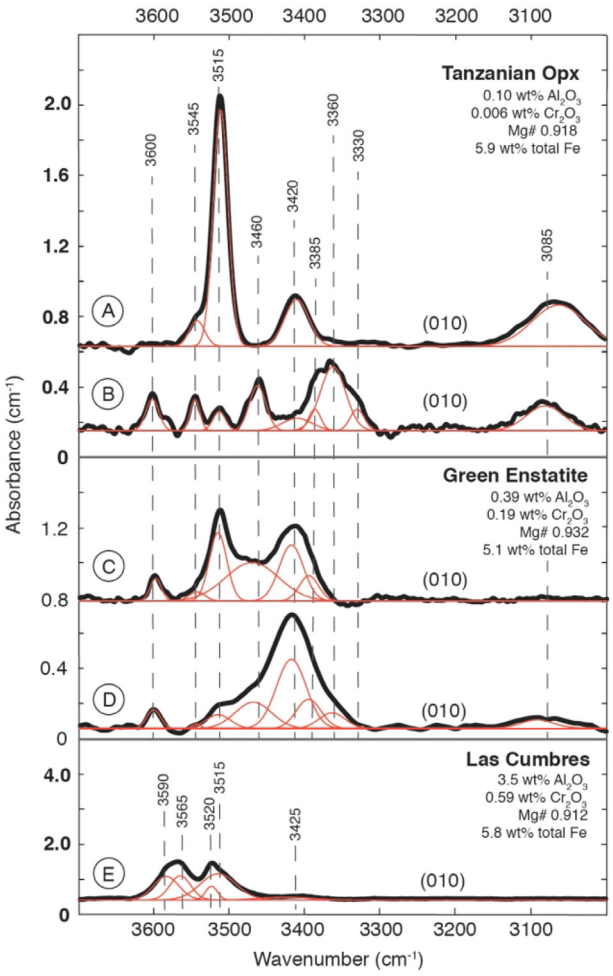

Fig. 2. Stacked FTIR spectra recorded using unpolarized light in the cores of four different types of orthopyroxene, heated or untreated, fitted into a series of Gaussian peaks. The Y-axis is offset for the different sample types. Mg/(Mg/Fe) and concentration of Al_2O_3, Cr_2O_3 and total Fe in wt.% obtained with EPMA are included for each type of orthopyroxene. The full chemistry is given in Appendix 1- Table A1. Tanzanian opx: A) core spectrum, untreated starting material, B) core spectrum following an experiment at 975 °C, ol-opx buffer, ~ΔQFM-1, 30 min. Green enstatite: C) core spectrum, untreated starting material, D) core spectrum following an experiment at 824 °C, ~ΔQFM-1, ol-opx buffer, 30 min. E) Core spectrum of a natural opx from a peridotite xenolith from Las Cumbres (EC_11, #10), Patagonia, discussed further in 4.2.1. The FTIR spectra from this figure are available in Supplementary data – S4.

3.2.1. Compositional dependence

In the Tanzanian orthopyroxene starting material, the main peak in FTIR spectra is at 3515 cm^{-1} – this is ~5x higher than those at 3545 cm^{-1}, 3420 cm^{-1} and 3085 cm^{-1}. Following experiments, the main peak is at 3360 cm^{-1} and peaks at 3330 cm^{-1}, 3420 cm^{-1} and 3600 cm^{-1} are also present. These are absent in the starting

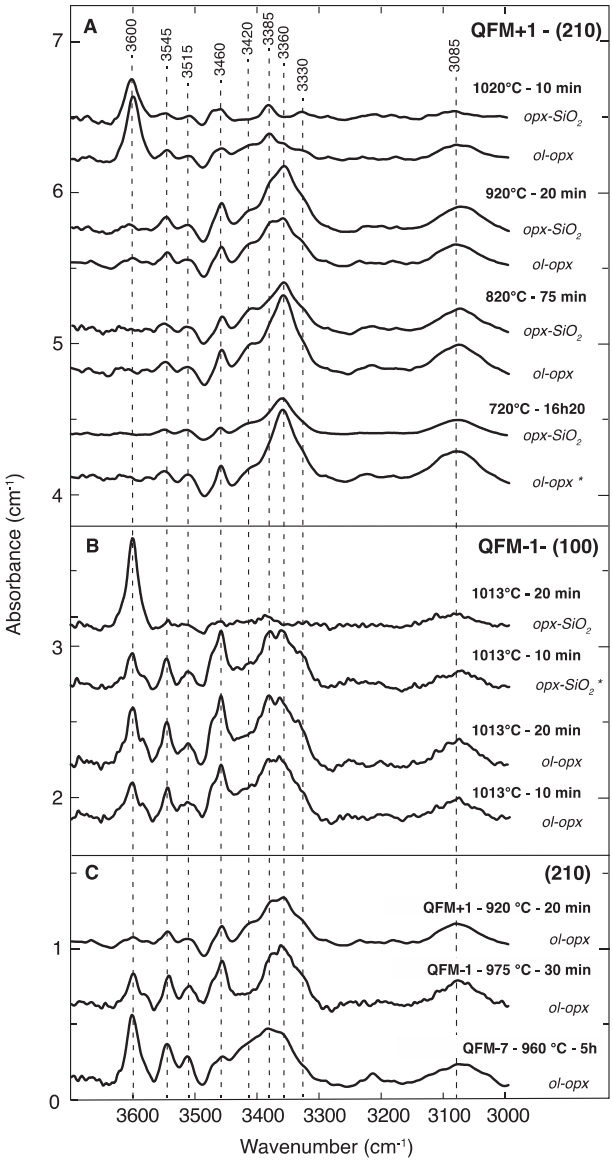

Fig. 3. Stacked FTIR spectra of measurements from crystal cores, following experiments with the Tanzanian opx at different temperatures, oxygen fugacity, orientation and silica activity. The measurements were made with unpolarised light. The core spectra were recorded from crystals showing profiles with a plateau at the core, except for the ones denoted with an asterisk*. A) Effects of the silica activity buffer and temperature: Experiments were run at ~ΔQFM + 1 and samples were prepared parallel to (210). Each pair of spectra shows a different experimental temperature, 720 °C, 820 °C 920 °C and 1020 °C, and compares the experiments made with ol-opx or ol-SiO_2 buffers. B) Effects of the a_{SiO2} buffers and the run length: The experiments were run at ~ΔQFM-1 and 1013 °C and oriented on (100). The two first spectra show the opx-SiO_2 experiments and the two last, the ol-opx buffer. C) Effect of oxygen fugacity: The experiments are oriented on (210) and run with the ol-opx buffer. They were run at different f_{O2}, (~ΔQFM-7, ~ΔQFM-1 and ~ΔQFM + 1), and at temperatures between 920 and 975 °C.

material spectrum (Fig. 1, Fig. 2). The green enstatite shows slightly different behaviour. Both heated (1-atm experiments) and untreated material show the same peaks (except the 3085 cm^{-1} peak, which appears only after heating), but with different relative peak heights. In the untreated material, the peak with the highest absorbance is at 3515 cm^{-1}, followed by 3420 cm^{-1} and 3460 cm^{-1} while for the heated material, the main peak is at 3420 cm^{-1} and the peak at 3515 cm^{-1} decreases considerably in intensity (Fig. 3). The 3385 cm^{-1}, 3420 cm^{-1}, 3460 cm^{-1} peaks appear to be slightly shifted towards higher wavenumbers. It is not clear if this is simply a peak shift, or if these actually represent different peaks and thus different defects. Unlike the Tanzanian opx, the 3600 cm^{-1} peak is present in both the starting material and heated material.

3.2.2. Influence of temperature and run length

The temperatures expressed here are experimental temperatures rather than analytical temperatures. The temperature influences the shape of the spectra in the OH stretching region (Fig. 3A). At greater temperatures, the height of the peaks reduces, except the peak at 3600 cm^{-1}. This peak is not present in experiments conducted below ~920 °C, but is increasingly visible at higher temperatures (Fig. 3A). This behaviour is observable at both ~ΔQFM-1 and ~ΔQFM + 1 (Fig. 3A and B). Run length also affects the absorbance intensity. Longer runs show a decrease in absorbance for all the peaks, except the 3600 cm^{-1} peak at T > 920 °C. Fig. 3B shows spectra from experiments run at 1013 °C with the opx-SiO_2 buffer for 10 and 20 min- all the peaks which were present following the 10 min experiment, are gone in the 20 min experiments, except for the peak at 3600 cm^{-1}.

3.2.3. Influence of silica activity

Fig. 3A shows a comparison of core spectra following experiments at ~ΔQFM + 1 with the ol-opx and opx-SiO_2 buffers, for the same temperatures and run times. Following experiments at T < 920 °C and a_{SiO2} buffered by either ol-opx or opx-SiO_2, the 3060 cm^{-1}, 3330 cm^{-1}, 3385 cm^{-1}, 3420 cm^{-1}, 3460 cm^{-1}, 3515 cm^{-1} and 3545 cm^{-1} peaks are all present in core spectra. At T≈920 °C, the 3600 cm^{-1} peak appears in addition to the other peaks. With the ol-opx buffer, at T ≥ 1000 °C, the 3545 cm^{-1}, the 3515 cm^{-1} and the 3085 cm^{-1} peaks seem to keep the same height as in spectra following experiments at lower temperatures, while other peak heights are relatively reduced. The 3600 cm^{-1} peak appears, and is relatively intense compared to the spectra from experiments at T≈920 °C. With the opx-SiO_2 buffer, at T ≥ 1000 °C, the 3600 cm^{-1} peak becomes the main peak, and has a significantly greater absorbance than the others. The 3460 cm^{-1}, 3385 cm^{-1} and the 3085 cm^{-1} peaks are barely discernable. Similar behaviour is also observed following 20 min experiments at ~ΔQFM-1 and 1013 °C in Fig. 3B. Following experiments at T < 920 °C, the spectra with the ol-opx and opx-SiO_2 buffer are quite similar but not above T > 920 °C. Only above this temperature is an effect of silica activity observable. Since the measurements in Fig. 3 are assumed to represent true cores (measurements from plateaus), this is unlikely to reflect a more advanced state of dehydration for the measurements with opx-SiO_2 buffer. However, the communication of external a_{SiO2} into the

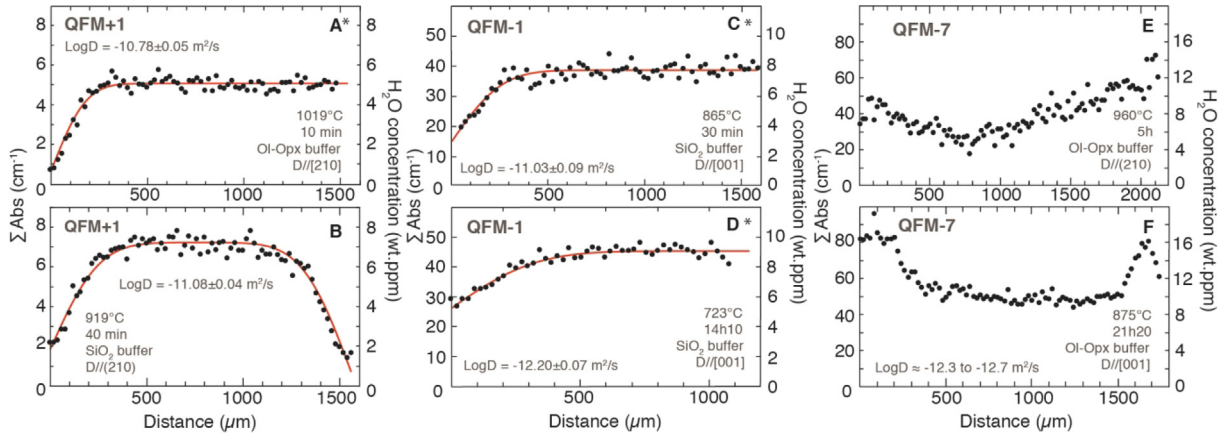

Fig. 4. Examples of processed hydrogen diffusion profiles. A and B are half and full profiles at ~ΔQFM + 1. C and D are half profiles at ~ΔQFM-1. E and F show a full profile for experiments at ~ΔQFM-7. Models for A, C and D were obtained by using, Eq. (1), model B with Eq. (2). Profiles with an asterisk (*) were mirrored for visualization purposes. H_2O concentrations were calculated using 0.067 x$\sum Abs_{1cm} \times 3$.

crystal cores, whilst maintaining an apparently constant H content, suggests the presence of a faster diffusing mechanism.

3.2.4. Influence of oxygen fugacity

By comparing the results of the 10 min experiments conducted with the ol-opx buffer above 1000 °C in Fig. 3A and B, it appears that the rearrangement of the peaks occurs to a greater extent at ~ΔQFM + 1 than at ~ΔQFM-1. Following the 10 min ol-opx buffered experiments at ~ΔQFM-1, all the peaks are present and the absorbance of the 3600 cm^{-1} peak is lower than the absorbance of the 3385 cm^{-1}, 3360 cm^{-1} and 3460 cm^{-1} peaks, whereas at ~ΔQFM + 1, the peaks heights have decreased and the absorbance of the 3600 cm^{-1} peak is greater than the absorbance of the 3385 cm^{-1}, 3360 cm^{-1} and 3460 cm^{-1} individually.

Fig. 3C shows a comparison between core spectra from ol-opx buffered experiments at different f_{O2} and temperatures within 55 °C. At ~ΔQFM-7, the absorbance of the 3600 cm^{-1} peak is greater than the absorbance of all the other peaks, and the 3420 cm^{-1} peak shows different behaviour than at ~ΔQFM-1 and ~ΔQFM + 1. The absorption associated with the different peaks, such as the 3420 cm^{-1}, 3385 cm^{-1} and 3360 cm^{-1} peaks, is comparable whereas at ~ΔQFM-1 to ~ΔQFM + 1 the absorption at 3420 cm^{-1} is much lower than absorption at 3385 cm^{-1} and 3360 cm^{-1} ($Abs_{3420} \ll Abs_{3385}$, Abs_{3360}). The experimental oxygen fugacity does not seem to change the position of the peaks but seems to partially affect the absorbance of certain peaks, such as 3420 cm^{-1} and 3460 cm^{-1}.

3.3. Hydrogen diffusion

3.3.1. Diffusion profiles – lengths and shapes

Following experiments at ~ΔQFM-1 and ~ΔQFM + 1, using the Tanzanian opx, $\sum$Abs profiles generally show error function shapes (Fig. 4 - A-D). Forty-nine profiles show a flat plateau in the core and 12 do not. All experiments conducted at ~ΔQFM-7 have an M shape, with

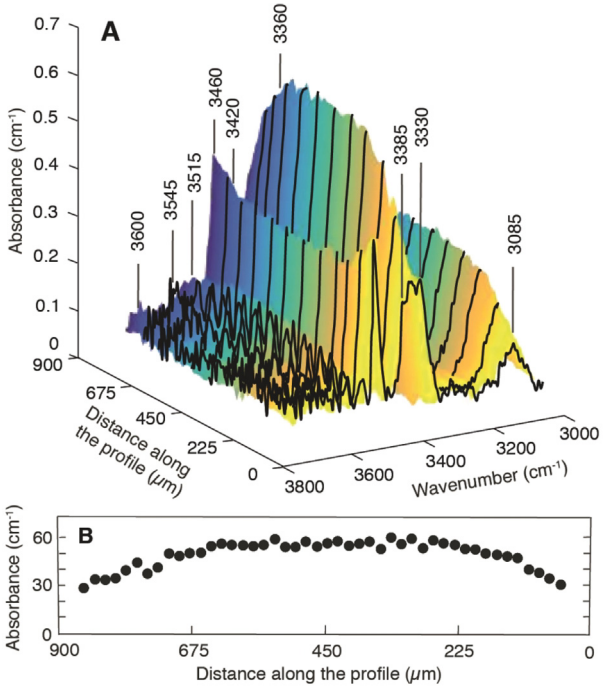

Fig. 5. A) 3D plot of the thickness normalized FTIR spectra along a hydrogen diffusion profile on an experiment on the Tanzanian opx, at 926 °C, ~ΔQFM-1, opx-ol buffer, 20 min and D//[001], showing that different peaks have different behaviours during hydrogen loss. For clarity reasons, the number of spectra (black lines) was down sampled by a factor 3. The color spectrum was also chosen only for clarity. On the distance axis, 0 is one edge of the crystal. Note that the absorbance of the 3460 cm^{-1} peak increases towards the rims where the absorbance of others decrease. B) Total absorbance variation across the crystal. The left-hand side of the plot is the edge of the crystal, as in panel A.

low concentrations at the core, increasing concentrations towards the rim and a decrease at the rim itself (Fig. 4 – E, F). The error function shaped profiles are consistent with simple diffusion, while M-shaped profiles implies more complex processes such as diffusion coupled to inter-site

reaction or depleting boundary conditions (Jollands et al., 2019). In the majority of experiments at ~ΔQFM-1 and ~ΔQFM + 1, the nine peaks, which were extracted from the peak fitting algorithm, do not show the same behaviour during diffusion, as shown in Fig. 5.

3.4. Diffusion coefficients

Hydrogen diffusion coefficients are presented in Table 1 for the ~ΔQFM + 1 and Table 2 for ~ΔQFM-1 and ~ΔQFM-7 experiments. The profiles not showing a flat plateau at the core were not included in further calculations. These profiles may be the product of several unconstrained factors, including, for example, the measurement of 1D profiles from a 3D crystal (Shea et al., 2015a). Additionally, the initial core concentrations could be higher or lower than what is observed, or could potentially show heterogeneity. Diffusion coefficients calculated solely from profiles showing a plateau at the core are shown in Fig. 6. For each main axis and the [210] direction, an activation energy (E_a) and a pre-exponential factor (D_0) was determined (Table 3) by weighted least-squares regression of all data (Eq. (4)) where R is the gas constant (kJ mol^{-1} K^{-1}) and T is the temperature in kelvins, except for ~ΔQFM-7 as there is not enough data to make an accurate calculation.

$$\log D = \log D_0 - E_a/(2.303RT) \quad (4)$$

At ~ΔQFM-1, the regressions for each direction shows that D//[001] > D//[100] > D//[010], with D//[210]≈ D//[100]. This was also observed by Carpenter (2003) following experiments using San Carlos enstatite, and by Stalder and Behrens (2006) on H-self diffusion experiments on synthetic enstatite. Anisotropy appears to increase at lower temperatures: log D//[001] minus log D//[010] is around 0.3 at 1000 °C, and 0.8 at 700 °C (Fig. 6A).

3.4.1. Effect of a_{SiO2}, f_{O2} and the starting material composition

For each a_{SiO2} buffers (ol-opx or opx-SiO_2), and for each main crystallographic axis, 95 % confidence envelopes were calculated. According to these, for D//[001] and D//[210], it is not possible to distinguish two statistically significant separate populations for the different buffers (Appendix 2 – Fig. B6). For D//[100], the two confidence envelopes do not overlap between ~800 °C and ~920 °C. The caveat is that the small number of data points for individual buffer-orientation pairs lead to fairly high uncertainties. Therefore, within uncertainties, the different a_{SiO2} buffers (ol-opx or opx-SiO_2) are unlikely to affect H diffusion coefficients (Fig. 6). Diffusivity appears to be slightly higher at

Table 3
Arrhenius parameters of the experiments at ~ΔQFM + 1, ~ΔQFM-1.

f_{O2}	Diffusion direction	Log D_0 (m^2/s)	E_a (kJ mol^{-1})
~ΔQFM-1	D//[100]	−5.11 (0.42)	139 (10)
~ΔQFM-1	D//[010]	−4.93 (0.57)	149 (13)
~ΔQFM-1	D//[001]	−5.52 (0.41)	125 (9)
~ΔQFM-1	D//[210]	−4.73 (0.21)	146 (5)
~ΔQFM + 1	D//[210]	−4.61 (0.31)	145 (7)

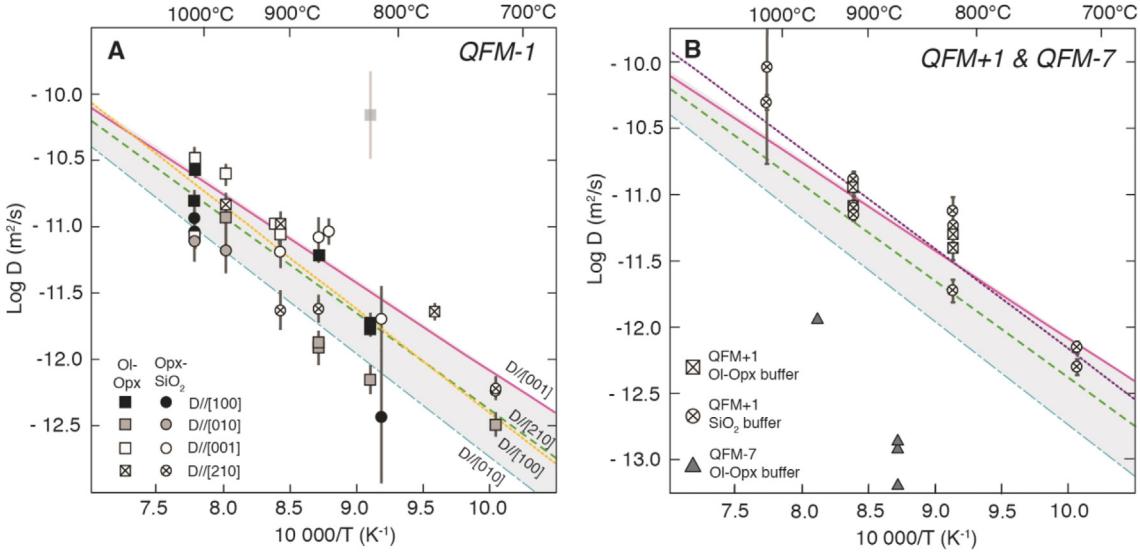

Fig. 6. Arrhenius diagrams of hydrogen diffusion of the Tanzanian opx at different f_{O2}. A) ~ΔQFM-1: Hydrogen diffusion along the three crystallographic axis directions (D//[100], D//[010] and D//[001] and along the [210] direction. The pink line, the green, blue and yellow dashed lines are the best fit to Eq. (4) for diffusion parallel to D//[001], D//[010], D//[100] and D//[210]. The outliers are shown as shaded symbols. B) ~ΔQFM + 1 and ~ΔQFM-7: Hydrogen diffusion along random orientations. The purple line is the best fit to Eq. (4) for ~ΔQFM + 1. The other lines are the best fits from experiments at ~ΔQFM + 1 (panel A), these are added for comparison.

~ΔQFM + 1 than ~ΔQFM-1, although the difference is within uncertainty (Fig. 6B). Four diffusion coefficients were estimated at ~ΔQFM-7: one at 960 °C and three at 875 °C (Fig. 6B). These experiments show lower diffusivities, potentially with a higher activation energy than the ~ΔQFM-1 and ~ΔQFM + 1 experiments. It is not possible, with our dataset, to explain the formation of the M-shaped profiles, so these data will not be discussed further.

Diffusion appears to be faster in the green enstatite than the Tanzanian enstatite. $Log_{10}D$ at ~825 °C varies between -11.8 ± 0.1 m^2/s and -10.1 ± 0.2 m^2/s for the green enstatite (D//[100] and D//[010]) and between -12.4 ± 0.5 m^2/s and -11.7 ± 0.24 m^2/s for Tanzanian orthopyroxene (D//[100], D//[010] and D//[001]) (Table 1). Further experiments would be necessary to test if these observations are systematic and reproducible.

4. DISCUSSION

4.1. Comparison with other H diffusion coefficients

Hydrogen diffusion coefficients in orthopyroxene using dehydration experiments on synthetic end member enstatite (e.g. Stalder and Skogby, 2003), R^{3+} cation doped enstatite (e.g. Stalder et al., 2007; Schlechter et al., 2012), H-^{2}H exchange experiments in synthetic enstatite (Stalder and Behrens, 2006), and also dehydration experiments on natural mantle orthopyroxene from San Carlos (Carpenter, 2003) and Kilbourne Hole (Stalder and Skogby, 2003) showed up to ~5 orders of magnitude variation in diffusion coefficients, likely the result of different diffusion mechanisms. Such variations between different experimental calibrations of H diffusion in NAMs is not uncommon – similar ranges have been shown for olivine, clinopyroxene and garnet (e.g. Demouchy and Bolfan-Casanova, 2016; Tian et al., 2017; Reynes et al., 2018 and references therein). These discrepancies have been suggested to represent either different diffusion pathways (e.g. Kohlstedt and Mackwell, 1998; Demouchy et al., 2006; Padrón-Navarta et al., 2014; Thoraval and Demouchy, 2014), and/or some complex interplay between diffusion and reaction (e.g. Jollands et al., 2019). In orthopyroxene, suggested reasons for the discrepancy are different crystal chemical chemistries, oxidation states of Fe (Stalder et al., 2007), and that the preferred H incorporation mechanism in synthetic and natural samples are different (Stalder and Skogby, 2007).

Diffusivities from experiments using pure, Fe-doped, Fe/Al-doped (except the Fe/Al experiments presented as the blue hexagons in Fig. 7A) and Cr-doped enstatite (Stalder and Skogby, 2003; Stalder and Behrens, 2006; Stalder et al., 2007; Schlechter, 2011) are relatively low in comparison to experiments conducted using natural samples

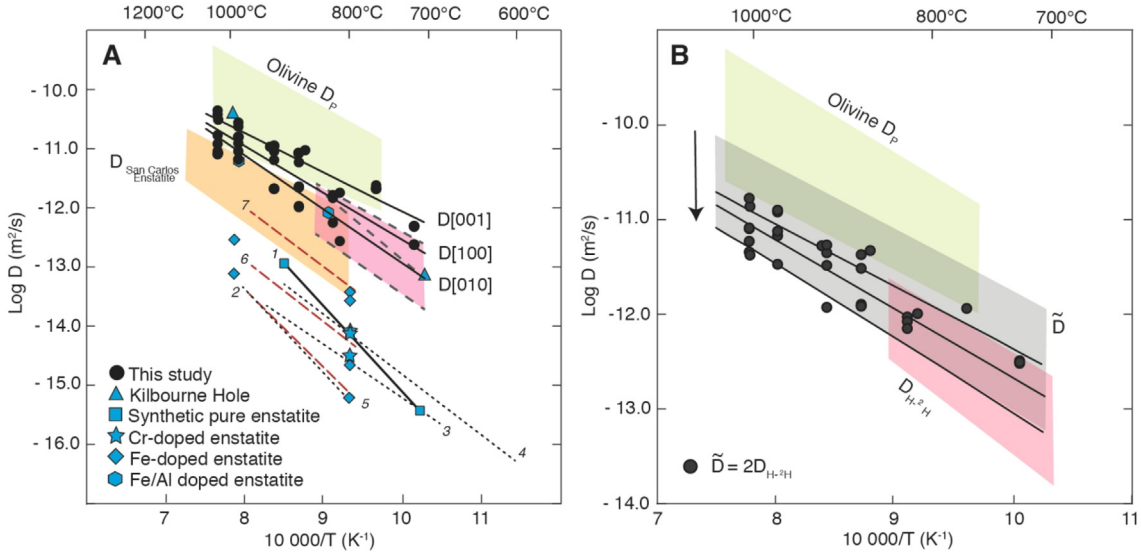

Fig. 7. A) Arrhenius diagram of hydrogen diffusion in opx at ~ΔQFM-1 from this study along with some hydrogen diffusion coefficients from the literature. The data from this study and their associated regressions are shown as black dots and lines, respectively (refer to Fig. 6A for more details). Blue squares and the solid black line (1) are from Stalder and Skogby (2003) (700 °C, 900 °C, 1-atm, in air, $E_a[010] = 295 \pm 55$-kJ/mol), blue diamonds from Stalder et al. (2007) (800 °C, 1000 °C, 1-atm, in air, [100]), blue stars from Stalder and Behrens (2006) (800 °C, 1-atm, [100], [010], [001]), blue hexagons (8.2 wt.% FeO, Fe_2O_3 n.a, 0.05 wt.% Al_2O_3) from Schlechter (2011) (829 °C-987 °C, [100], 1-atm, in air), blue triangles from Stalder and Skogby (2003) (700 °C, 1000 °C (D calculated from Bell et al., 1995 for 1000 °C), 1-atm, $E_a[001] = 213 \pm 47$ kJ/mol), the yellow field from Carpenter (2003) (800 °C to 1100 °C, 1-atm, ~ΔQFM-0.4 to ~ΔQFM-4.60, $E_a[100] = 127 \pm 17$ kJ/mol, $E_a[010] = 197 \pm 19$ kJ/mol, $E_a[001] = 161 \pm 17$ kJ/mol) and the light pink field is H self-diffusion for [100], [010] and [001], from Stalder and Behrens (2006) The dotted black lines are Fe-doped experiment with x_{Fe} varying: 2) Fe# =0.01 (Stalder and Skogby, 2007), 3) and 4), Fe# =0.040 and 0.019 respectively (Stalder et al., 2007). The dashed red lines are Fe/Al-doped experiments from Schlechter (2011): 5) 7.3 %wt Al_2O_3, 6) 1.9 wt.% FeO, 0.2 wt.% Fe_2O_3, 0.5 wt.% Al_2O_3, 7) 2.7 wt.% FeO, 0.8 wt.% Fe_2O_3, 0.3 wt.% Al_2O_3). Also shown is the proton-polaron (D_P) diffusivities in olivine from Kohlstedt and Mackwell (1998) in the light green field. The outliers of Fig. 6 (panel A) are not shown for clarity. B) Arrhenius plot of the relation between the D_P and D_{H-^2H}. The grey field represents the data from this study at ~ΔQFM-1 shown in panel A. The pink and green fields are the same as for panel A. (For interpretation of the references to colour in this figure legend, the reader is referred to the web version of this article.)

(Stalder and Skogby, 2003; Carpenter, 2003) and diffusivities associated with H-^{2}H exchange (Stalder and Behrens, 2006), falling into the range of diffusivity likely associated with diffusion of metal (M) vacancies (Fig. 7A. The exception is the sample of Schlechter et al. (2012) containing 8.2 wt.% FeO, Fe_2O_3 n.a, 0.05 wt.% Al_2O_3 (blue hexagons in Fig. 7A) show higher diffusivities which are in line with previous findings on the enhancing effect of iron on hydrogen diffusivity (Stalder and Skogby, 2007), but slower than H self-diffusion (Stalder and Behrens, 2006) as Fe # < 0.10 (Stalder et al., 2007). The self-diffusivity of H measured by H-^{2}H exchange ($D_{H-\ ^2H}$) derived from experiments using pure enstatite are similar, but slightly slower, than what we observe.

Results from experiments on natural mantle orthopyroxene also show some disparities. The dehydration experiments on the San Carlos orthopyroxene (Carpenter, 2003), performed at ~ΔQFM-0.4 to ~ΔQFM-4.6, show slower diffusivities than the one of Kilbourne hole (Stalder and Skogby, 2003) and those from this study. This is potentially due to a relatively low $Fe^{3+}/\sum Fe$ in the crystals or to a larger amount of Al than the Tanzanian orthopyroxene and the Kilbourne Hole enstatite (Appendix 1 – Table A1), as discussed for synthetic samples (Stalder et al., 2005; Stalder and Behrens, 2006; Schlechter et al., 2012). Carpenter (2003), Stalder et al. (2005) and Kohn et al. (2005) also suggests that the presence of a trivalent cation with only one oxidation state inhibits the ability of Fe or Cr to take part in the redox reactions that facilitate hydrogen diffusion.

The diffusivities determined following experiments using Kilbourne Hole orthopyroxene (Stalder and Skogby, 2003) and from this study are similar (although slightly slower) to those of the fastest known hydrogen diffusivity in olivine (Kohlstedt and Mackwell, 1998), suggesting a mechanism akin to the proton-polaron exchange (D_P; Kohlstedt and Mackwell, 1998) (Fig. 7A, B). In this mechanism, H moves through the crystal by reducing Fe^{3+}, generically described as $H_i^{\cdot} \longleftrightarrow h^{\bullet}$, where $h^{\bullet}$ is a polaron (electron hole).

The chemical diffusivity describing the uptake of hydrogen in olivine is described by the relation $\widetilde{D} \approx (2D_p + D_{H-\ ^2H})/(D_p + D_{H-\ ^2H})$ from Kohlstedt and Mackwell (1998), where $\widetilde{D}$ is the diffusivity that is directly measured in experiments, D_p and $D_{H-\ ^2H}$ and the diffusivities of polarons and hydrogen ions, respectively. Assuming that $D_p \gg D_{H-\ ^2H}$ this relationship becomes $\widetilde{D} \approx 2D_{H-\ ^2H}$ (Kohlstedt and Mackwell, 1998). Accordingly, we subtracted 0.3 log units from our log D. The resulting diffusivities agree well with the field of the H self-diffusion coefficient of Stalder and Behrens (2006) on synthetic pure enstatite, which is coherent with the relationship observed by Kohlstedt and Mackwell (1998) in olivine (Fig. 7B). By assuming that the same relationship is applicable to orthopyroxene and that the diffusivities we measured are associated with the proton-polaron mechanism, this can explain why the diffusivities we measured are higher than all the others, except for the Kilbourne Hole samples (Fig. 7A), and only slightly different from the H self-diffusion experiments (Fig. 7A, B). The diffusivities of the proton-polaron exchange should be higher than $D_{H-\ ^2H}$, which is the case in the present study and the Kilbourne Hole samples.

In summary, on the basis of a broadly similar behaviour of olivine and orthopyroxene, our results support the idea that the diffusivities we measured represent the proton-polaron exchange based on the comparison with the H-self diffusivities recorded by Stalder and Behrens (2006). It is also worth emphasizing that, if our interpretations are correct, the proton-polaron mechanism is still active at ~ΔQFM-1, which would be equivalent to a relatively reducing mantle environment.

4.2. Water retention in natural orthopyroxene

4.2.1. Application to mantle xenoliths

As a demonstration of the application of this new diffusion data, we calculated time scales using H concentration profiles in a natural orthopyroxene from a mantle xenolith (Las Cumbres, Chile). A single crystal of orthopyroxene (composition in Fig. 2e) was extracted from a mantle xenolith sample (EC_11) from an alkali basalt flow (~48 wt.% SiO_2, Mg# 0.65). FTIR mapping shows a decrease in hydrogen from core to rim in the upper part of the crystal (Fig. 8), which could be attributed to either H diffusion or H charge balancing element such as Al or Cr which might show zonation (Tollan et al., 2015; Tollan et al., 2019). To test the latter possibility, EPMA-WDS maps of the same crystal area were recorded. The maps show essentially homogenous concentrations of all elements that have been invoked for charge balancing of H (Al, Fe, Cr; Fig. 8). The Ca map shows homogeneity where the dehydration profile has been observed, but heterogeneity in the lower part of the crystal, which suggests to think that the bottom half might have been recrystallized. In short, it appears that H is decoupled from these elements, suggesting that the H profiles were likely generated by diffusion. The measured absorbance on the map was thickness-normalized with the Si-overtones and converted to wt. ppm of H_2O.

Using the relationship $0.067 \times \sum Abs_{1cm} \times 3$, the core has a concentration of ~26 wt. ppm H_2O and the rims ~5 wt. ppm H_2O. As above, this is likely an underestimate given that the baseline correction removes broad bands. Since the measured core does not display a distinct plateau, it is not clear to what degree this concentration reflects the initial equilibrium H_2O content, which is a necessary input for diffusion modelling. One method of estimating this is to use the H_2O content of co-existing clinopyroxene and the subsolidus equilibrium partition coefficient, $D_H^{cpx/opx} \approx 2$ (e.g. Peslier et al., 2002; Xia et al., 2010; Denis et al., 2015; Demouchy and Bolfan-Casanova, 2016). Clinopyroxene crystals from the same sample were measured by FTIR spectroscopy and give concentrations of ~65 wt. ppm H_2O (using an absorbance coefficient of 0.141 from Bell et al. (1995) which indicate $D_H^{cpx/opx}$ of ~3 instead of 2, which could indicate that the orthopyroxene initial concentration was modified. However, one has to be careful about the initial clinopyroxene concentrations as H diffusion coefficients for clinopyroxene (Woods et al., 2000; Ferriss et al., 2016) are of the same order as orthopyroxene, and may therefore also have been affected by fast diffusion.

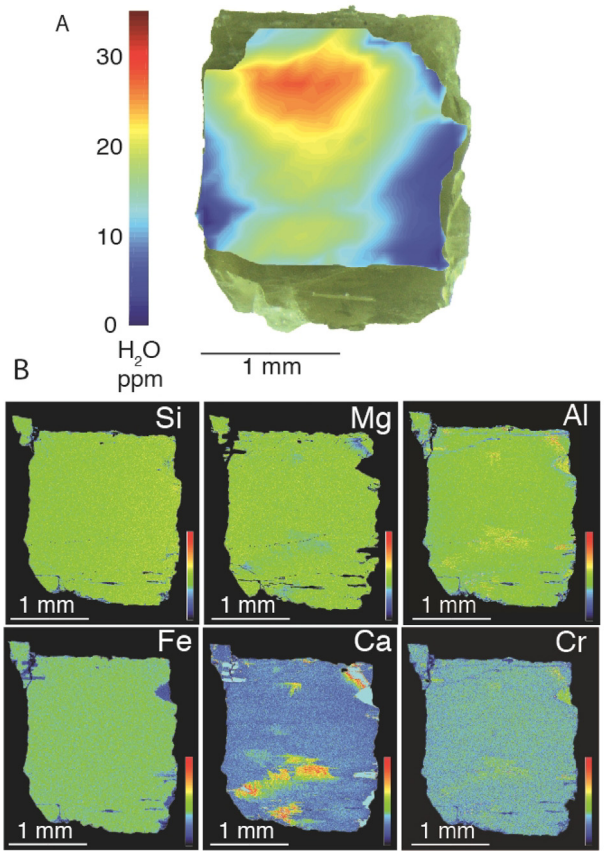

Fig. 8. Mantle orthopyroxene crystal (2 × 2.3 mm) from sample EC_11 from Las Cumbres, Patagonia. (A) FTIR map of the water concentration, superposed on the crystal analyzed. Water contents were estimated based on $\sum Abs_{1cm} \times 0.067 \times 3$; (B) Qualitative EPMA maps of major elements.

Therefore, because we do not have an accurate determination of the initial (or at least, pre-dehydration) H content of the orthopyroxene, three different initial core compositions $C_{core,t=0}$ were chosen, representing the measured concentration (26 wt. ppm H_2O) a concentration that is an approximate average of orthopyroxene in mantle xenoliths, 200 wt. ppm H_2O (Demouchy and Bolfan-Casanova, 2016) and an intermediate concentration (100 wt. ppm H_2O).

H diffusion was modelled at a temperature of 1200 °C, corresponding to the temperature of the host magma for alkaline systems (e.g. Nekvasil et al., 2004). A second, colder, temperature of 1100 °C was used for comparison purposes. Diffusion coefficients were extrapolated to these temperatures based on the E_a and D_0 of D//[010] and D//[001] (Table 3) determined in this study. A transect crossing the high H concentration zone on the FTIR map (Fig. 9A) was used for modelling. Boundary conditions were not fixed, but instead allowed to vary during the fitting routine. Data were fitted to Eq. (1) using an explicit finite difference method, and minimum times of ascent were calculated with $\log_{10}D = -10.3$ to -10.5 m^2/s at 1100 °C and $\log D = -9.9$ to -10 m^2/s at 1200 °C, assuming hydrogen loss upon ascent, with a constant composition at the crystal rim. The results are detailed in Table 4 and vary between 0.3 h to 10.5 h. For comparison, the same calculations were made, with initial concentrations of 26 wt. ppm H_2O and 200 wt. ppm H_2O, using the fastest and slowest coefficients measured by Carpenter (2003) on the mantle orthopyroxene from San Carlos (Fig. 7). The results are on the same order of magnitude as the ones from this study, up to one order of magnitude higher for the slowest scenario (D// [010], $C_{core,t=0} = 200$ wt. ppm H_2O, T = 1100 °C) (Table 4), varying from 0.7 h to 147 h. Even using the lower diffusivities, the timescales are still shorter than those from Fe-Mg inter-diffusion in olivine (described below). The diffusion coefficients for the Kilbourne Hole enstatite (Stalder and Skogby, 2003) were not used for comparison because they are sufficiently well constrained to extrapolate to higher temperatures.

Timescales were also extracted from Fe-Mg diffusion profiles in olivine (e.g. Dohmen et al., 2007; Dohmen and Chakraborty, 2007), from the same xenolith sample (EC_11), in contact with the host magma. Fe-Mg zoning profiles were observed with backscattered electron (BSE) imaging at the contact of the host-basalt with olivine crystals at the edge of the xenoliths from the same locality as EC_11. Fe-Mg inter-diffusion was then modelled, with the inputs for the simulations based on the spinel peridotite field: (1) pressures between 1 to 2 GPa (Green and Ringwood, 1967), (2) oxygen fugacities between ΔQFM = +1 to ΔQFM = −2 (compilation in Frost and McCammon (2008) and references therein), (3) magma temperatures of 1200 °C to 1100 °C (Nekvasil et al., 2004). To cover a possible range of formation of the profiles, two scenarios, one with the parameters associated with the lowest diffusivities, T = 1100 °C, P = 2 GPa, f_{O2} = ΔQFM = −2 and $D_{Fe\text{-}Mg,[100]}$, and one with the parameters associated with the highest diffusivities, T = 1200 °C, P = 1 GPa, f_{O2} = ΔQFM=+1 and $D_{Fe\text{-}Mg,[001]}$, were calculated using 16 profiles (Fig. 9A). $D_{Fe\text{-}Mg}$ were calculated from Dohmen and Chakraborty (2007). We do not have information regarding the orientations of the olivine grains, so we calculated timescales assuming diffusion along both the fastest ($D_{[001]}$) and slowest axes ($D_{[010]} \approx D_{[100]}$) (Dohmen et al., 2007) in order to encompass the entire range of possible D values. These timescales are maximum values as they assume that no initial growth zonation was present. The calculated times vary between 10.8 to 126 years for the slowest model and between 0.12 to 0.99 years (42 to 361 days) for the fastest model (Fig. 9B). The order of magnitude difference within each scenario can be due to variability of the assumed orientation of the olivine grains in the model. The model naturally assumes that Fe-Mg diffusion starts at the exact moment of entrainment, and that there is no time lag (as discussed by Cheng et al. (2020) albeit for a magma chamber setting).

Distinguishing between profiles formed solely due to diffusion, or growth from an evolving system, or a combination of the two processes is challenging (Shea et al., 2015a; Shea et al., 2015b), with potential lines of evidence coming from (1) isotopic fractionation (Sio et al., 2013; Oeser et al., 2015), (2) anisotropy; or (3) relative diffusivities between different elements (Gordeychik et al., 2018; Mutch et al., 2019). We use the latter - the first order assumption is

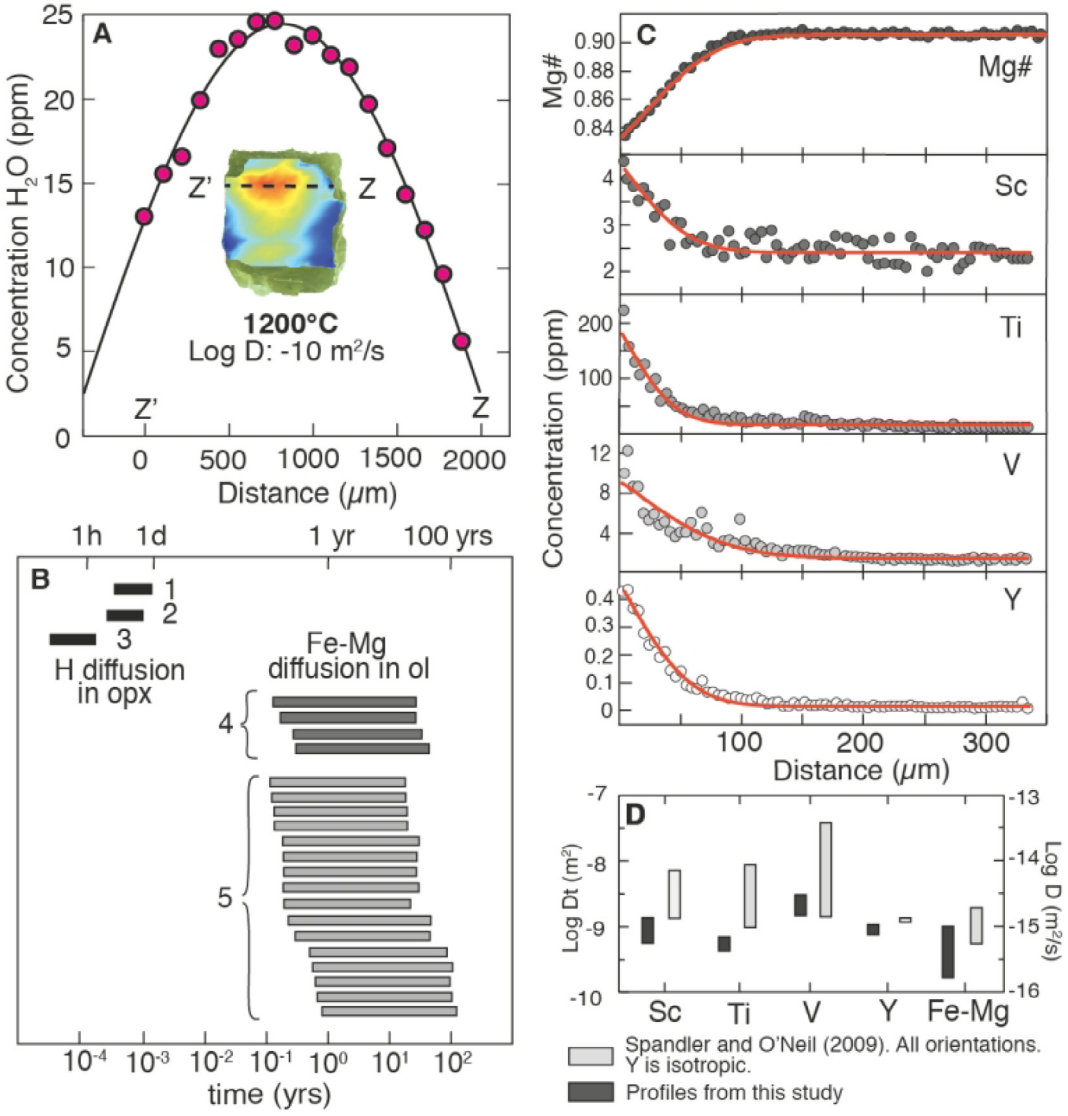

Fig. 9. (A) Sample EC_11: Profile Z'-Z and the solution to Eq. (1) fitted to the data for 1200 °C and log D = -10 m^2/s (D//[010]). For $C_{core,t=0}$ of 26 wt. ppm H_2O, 100 wt. ppm H_2O and 200 wt. ppm H_2O, the calculated times are 0.3 h, 2.8 h and 3.9 h. Fits to Eq. (2) for 1100 °C, log D = −10.5 m^2/s (D//[010]) and for initial $C_{core,t=0}$ of 26 wt. ppm H_2O, 100 wt. ppm H_2O and 200 wt. ppm H_2O give calculated times of 1.3 h, 7.6 h and 10.5 h. (B) Comparison between the modelled times of ascent using H diffusion in orthopyroxene and Fe-Mg diffusion in olivine. 1, 2 and 3: H diffusion in orthopyroxene for $C_{core,t=0}$ = 26 wt. ppm H_2O, 100 wt. ppm H_2O and 200 wt. ppm H_2O respectively. 4: Fe-Mg diffusion in olivine in sample EC_11 (same as in A). 5: Fe-Mg diffusion in olivine for other samples from the same xenolith suite (EC). (C) Mg#, Sc, Ti, V and Y profiles on an olivine grain on sample EC_11 suggesting diffusion instead of growth zoning. The profiles were fitted with an analytical solution to Eq. (1) to extract Dt as the time of diffusion is unknown. (D) Comparison of the Dt calculated from the profiles in (C) with D calculated from experimental diffusion coefficients from Spandler and O'Neill (2009) on experiments where t = 25 days. The data used in this figure can be found in the Supplementary data – S5.

Table 4
Minimum times of ascent calculated for the Tanzanian opx and the San Carlos enstatite for two initial core concentrations (wt. ppm H_2O) for temperatures of 1100 °C and 1200 °C.

	T = 1100 °C		T = 1200 °C	
Starting material	$C_{core,t=0}$ = 26	$C_{core,t=0}$ = 200	$C_{core,t=0}$ = 26	$C_{core,t=0}$ = 200
Tanzanian opx	0.8 h–1.3 h	7.3 h–10.5 h	0.3 h–0.5 h	3.2 h–3.9 h
San Carlos enstatite*	1.7–17 h	14.5–147 h	0.7–5 h	6.5–46 h

* Diffusion coefficients parallel to [001] (fastest D) and [010] (slowest D) from Carpenter (2003).

that if elements with different experimentally determined diffusivities have the same length scale in a natural crystal, then the profile is unlikely to have been resulted solely from diffusion. Therefore, trace elements (Ti, Sc, V, Y) were measured using linear LA-ICP-MS scans at the edges of crystals where BSE zoning is visible. The measured profiles have error function forms, thus were fitted to Eq. (2) to extract Dt (diffusion coefficient (D) multiplied by time (t)). The trace element profiles show different lengths (Fig. 9C), with $D_Vt > D_Yt$, $D_{Sc}t$, $D_{Ti}t > D_{Mg\text{-}Fe}t$ (Fig. 9D), suggesting diffusive fractionation between the trace elements – these relative Dt are broadly consistent with the relative Dt from Spandler and O'Neill (2010). Therefore, the Fe-Mg and trace element zonings appear to be related to diffusion rather than to growth zoning, although a contribution from growth zonation cannot be discounted.

Regardless of the high variability within timescales from each method, the time scales calculated with the H diffusion in orthopyroxene and Fe-Mg diffusion in olivine are different by at least three orders of magnitude (Fig. 9B). H diffusion in opx gives times in the order of minutes to days whereas Fe-Mg diffusion in olivine gives times from a year to ~100 years.

If we assume, based on the arguments presented above, the end-member scenario that the Fe-Mg in olivine time scales are diffusion time scales, then the most likely explanation for the time scale discrepancy is that the two methods record different processes. A proposed history of the xenolith is shown in (Fig. 10), and described herein. Prior to exhumation, the peridotite sample EC_11 was likely equilibrated in the upper mantle at a temperature of around 830–850 °C (based on two pyroxene thermometry from Brey and Köhler (1990) and Al in olivine thermometry from De Hoog et al. (2010) and a pressure between 1 GPa and 2 GPa, based on the presence of spinel and absence of garnet (e.g. Ziberna et al., 2013). The initial H_2O content and the Mg# of the different minerals will be that of the lithospheric mantle, i.e. Mg# of 0.89–0.91 (McDonough, 1990), 10–140 wt. ppm H_2O (Demouchy and Bolfan-Casanova, 2016) (Fig. 10a). Once the xenolith is sampled, a chemical potential gradient in Fe-Mg is formed between the olivine and host magma, so diffusive exchange of Fe-Mg begins. At the same time, H diffusion in orthopyroxene is so fast that the crystal will be re-equilibrated with the magma (Fig. 10b) For a 2 mm orthopyroxene crystal, using the diffusivities from this study, just 1 to 3 h at 1100–1200 °C is needed to fully equilibrate the hydrogen content of the orthopyroxene with the magma (Appendix 2 – Fig. B7). These results are concordant with the re-equilibration times calculated for olivine, clinopyroxene and orthopyroxene (Padrón-Navarta et al., 2014; Ferriss et al., 2016; Lynn and Warren, 2020). This resulting H content could be higher or lower than the initial mantle signature. In this case, the magma is likely not to be totally anhydrous due to the close proximity (~50–100 km) of the orogenic volcanic arc in Patagonia. Tollan et al. (2015) and Ferriss et al. (2016), suggest that, when transported by H_2O-rich magmas, H-loss diffusion profiles in olivine and clinopyroxene develop only in the final stages of ascent, once the melt achieves volatile saturation (typically 2–3 km). Since our study and that of Stalder and Behrens (2006) indicate that H diffusion in orthopyroxene is similarly fast, it should

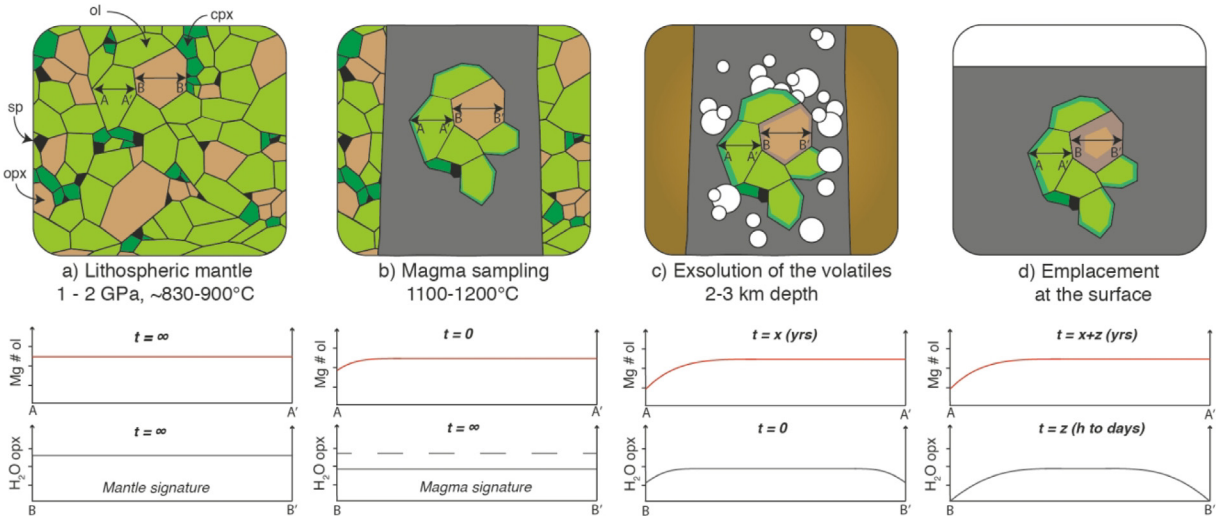

Fig. 10. Cartoon of the suggested history of the mantle xenolith EC_11, Las Cumbres, Patagonia and the associated Mg# in olivine and H_2O content in orthopyroxene evolution through time (Fig. 8, Fig. 9). (A) The mantle starting material is a spinel lherzolite, containing olivine (ol), orthopyroxene (opx), clinopyroxene (cpx) and spinel (sp), with a temperature of 900–1000 °C, at 1–2 GPa, or ~30 to 60 km depth. The profiles are flat as the peridotite minerals are in equilibrium. (B) Pieces of the starting material are sampled by an ascending basaltic magma, with temperature of 1100–1200 °C, a certain volatile content and f_{H20}. Fe-Mg inter-diffusion in olivine in contact with the host magma leads to formation of a Fe-Mg diffusion profile, which is going to be built over 0.5 to 100 years (t = x). The profile is asymmetric as the basalt is in contact with olivine on only one side. The H content in orthopyroxene is re-equilibrated with the magma within 1.5 h to 3 h for temperature of 1100 °C and 1200 °C. C) The host magma exsolves volatiles during the last step of the ascent, at shallow depths (2–3 km) (Ferriss et al., 2016; Tollan et al., 2015). H diffusive loss in orthopyroxene is activated, these profiles develop rapidly given the high diffusivity of H (Fig. 7). The profiles are created over 0.5 h to several hours (t = z) until the emplacement, where the diffusion profiles are quenched. The Fe-Mg inter-diffusion profiles do not change much in step c) given the low Fe-Mg diffusion coefficients (D ~10^{-16}–10^{-18} (Dohmen et al., 2007)).

respond similarly (Fig. 10c). The short duration of the final ascent following volatile exsolution may be (too) fast to major element zonation to develop ($D_{Fe\text{-}Mg}$ ~10^{-16} –10^{-18} m^2/s between 1100 °C and 1200 °C (Dohmen et al., 2007). After the emplacement and cooling of the lava flow, the hydrogen diffusion and Fe-Mg inter-diffusion profiles are frozen in, and record the timescales of two different processes (Fig. 10d).

To summarize, we suggest that the time-scale extracted from Fe-Mg inter-diffusion in olivine (months to years) record the ascent time following early differentiation of the host magma, whereas the timescales recorded by H diffusion in opx (hours) record the time elapsed between volatile exsolution and final cooling following emplacement. This indicates that H diffusion in orthopyroxene is recording only the final stages of ascent (following volatile exsolution) rather than the time between initial entrainment and eruption. This also includes the time taken to cool the lava flow on the surface although, in this case, the field relations did not allow us to determine the position of the xenoliths nor the thickness of the lava flow – there remains the possibility that the entire diffusive H-loss could have occurred within the lava on the Earth's mantle. It is important to note that this may not be the case in all magmatic systems. In order to correctly interpret H diffusion timescales, a good understanding of the initial mantle and primary magma H_2O contents is important. If the magma is anhydrous, the chemical potential gradient in H_2O (and thus diffusion of H) will likely develop immediately from the sampling of the xenolith by the host magma, therefore, recording the whole ascent process. In a more hydrous magma, the H_2O content of the xenolith will be buffered for much of the ascent, until a volatile phase is exsolved at shallow pressure, triggering late stage diffusion of H between crystals and melt.

4.2.2. Application to volcanic systems

The application of H diffusion coefficients, extracted from a non-mantle starting material, to H profiles extracted from mantle orthopyroxene can be questionable. A major difference is in the Cr and Al contents - the Tanzanian orthopyroxene has low Al (0.10 wt.% Al_2O_3) and Cr (0.006 wt.% Cr_2O_3) contents in comparison to the natural mantle orthopyroxene from this study (3.5 wt.% Al_2O_3 and 0.59 wt.% Cr_2O_3) (Fig. 2). As discussed previously, an increasing content of Al and Cr increases hydrogen solubility (Rauch and Keppler, 2002) and decreases the rate of hydrogen diffusion (Schlechter, 2011). The times of ascent calculated in the previous section using the Ds presented in this study are therefore minima.

While NAMs from mantle systems have gathered the most attention in previous work, an increasing number of studies report measurements of H in NAMs from magmatic systems (e.g. Wade et al., 2008; Weis et al., 2015; Edmonds et al., 2016; Lloyd et al., 2016; Turner et al., 2017; Nazzareni et al., 2020). During differentiation, crystallization of Cr-spinel and plagioclase result in strong depletions of Cr and Al in the melt respectively, leading to the crystallization of orthopyroxene (and other NAMs) with much lower Cr and Al than found in the upper mantle. For example, Edmonds et al. (2016) measured H_2O in orthopyroxene from an arc andesite which contained ~0.5–0.6 wt% Al_2O_3 and < 0.1 wt% Cr_2O_3 (Edmonds et al., 2016), concentrations much more similar to the orthopyroxenes in our experiments than typical mantle orthopyroxene. We note that these magmatic orthopyroxenes also have much larger Fe concentrations (23–25 wt.% FeO_T) which may make application of H diffusion rates from less Fe-rich crystals difficult (Stalder et al., 2007). However, the Fe content of the crystals used in this study is only slightly below than the critical threshold at which H self-diffusion is rate-limiting (Fe# ~0.10; Stalder et al., 2007). Hence, the effect of Fe on diffusion rates between the crystals studied here and those growing from more evolved magmatic systems may be small. Further work on such Al and Cr-poor and Fe-rich pyroxene compositions will be important in confirming this.

4.3. Retention of mantle water contents

In line with previous studies (Stalder and Behrens, 2006; Tian et al., 2017; Denis et al., 2018; Xu et al., 2019), we show that H diffusion in orthopyroxene is sufficiently rapid that complete re-equilibration of H_2O signatures is entirely plausible during entrainment and ascent in the host magma. In most spinel or garnet peridotites from mantle xenoliths, olivine is either dry or contains low amounts of water (<35 wt. ppm H_2O). Combined with the well-established rapid diffusivity of H in olivine (e.g. Mackwell and Kohlstedt, 1990; Kohlstedt and Mackwell, 1998; Demouchy and Mackwell, 2003; Du Frane and Tyburczy, 2012), olivine is traditionally considered as an unreliable recorder of mantle water contents (e.g. Denis et al., 2013; Demouchy and Bolfan-Casanova, 2016; Satsukawa et al., 2017). Pyroxenes on the other hand have previously been considered to be more likely to faithfully record their initial water signatures (Gose et al., 2009; Peslier, 2010; Xia et al., 2010; Warren and Hauri, 2014; Demouchy and Bolfan-Casanova, 2016; Xia et al., 2019), given that they have higher concentrations of water, 10 to 460 wt. ppm H_2O for opx and cpx (Demouchy and Bolfan-Casanova, 2016), and often show equilibrium orthopyroxene-clinopyroxene H_2O partitioning. Furthermore, they rarely show H diffusion profiles (currently six studies: Tian et al., 2017; Denis et al., 2018; Tollan and Hermann, 2019; Xu et al., 2019, Wang et al., 2021; this study). Our data supports previous suggestions that orthopyroxene is not necessarily a robust recorder of the original mantle H_2O content (Tian et al., 2017; Schmädicke et al., 2018; Denis et al., 2018; Tollan and Hermann, 2019). Indeed, the faster H diffusion rates measured here suggest that orthopyroxene at least has the potential to be even less reliable than these earlier studies suggested.

5. CONCLUSION

Hydrogen diffusion in orthopyroxene has the possibility to be sufficiently fast that the original water signatures of mantle orthopyroxene can be modified. It is relatively insensitive to a range of a_{SiO2} and f_{O2} representative for

the upper mantle. The results of our experiments suggest an important role for the proton-polaron exchange in orthopyroxene at relatively reducing conditions and support the relation $\widetilde{D} \approx (2D_p + D_{H-\ ^2H})/(D_p + D_{H-\ ^2H})$ established for olivine by Kohlstedt and Mackwell (1998). The experimentally determined hydrogen diffusivities of the Kilbourne hole mantle orthopyroxene (Stalder and Skogby, 2003) are similar to our results, but different from hydrogen diffusivities of San Carlos orthopyroxene (Carpenter, 2003). This implies an important role of the Fe^{3+}/Fe ratio in orthopyroxene for the proton-polaron exchange.

The application of these data, as well as previous determinations of diffusivity, may not be limited to mantle settings. The low Al and Cr contents of the starting materials used in our experiments are similar to compositions of orthopyroxene in mafic to intermediate magmas. Hence, hydrogen diffusion as determined in this experimental study may be useful in decoding temperatures and timescales from hydrogen profiles in more evolved magmatic systems. Future work focusing on diffusion of hydrogen in orthopyroxene in H_2O bearing magmas, under conditions appropriate to such systems (particularly the effect of f_{H2O}) will be necessary to accurately determine temperature and timescales from hydrogen diffusion in orthopyroxene. Such studies could further constrain potential volatile loss or gain from melt inclusions in orthopyroxene in volatile bearing magmas.

Declaration of Competing Interest

The authors declare that they have no known competing financial interests or personal relationships that could have appeared to influence the work reported in this paper.

ACKNOWLEDGEMENTS

Technical assistance with the EPMA from Martin Robyr and Arnaud Devoir, with the EBSD from Pierre Vonlanthen, and with the LA-ICP-MS from Alexey Ulianov is greatly appreciated. This research was supported by the Swiss National Science Foundation (SNF), grant numbers 20021-162666 and 200020-156421 to OM. We gratefully acknowledge the reviews of Roland Stalder and Anne Peslier, as well as editorial handling by the Editor Jeffrey G. Catalano, which substantially improved the presentation.

APPENDIX A. SUPPLEMENTARY MATERIAL

Supplementary data to this article can be found online at https://doi.org/10.1016/j.gca.2021.04.005.

REFERENCES

Aizawa Y., Barnhoorn A., Faul U. H., Fitz Gerald J. D., Jackson I. and Kovács I. (2008) Seismic properties of Anita Bay dunite: An exploratory study of the influence of water. *J. Petrol* **49**, 841–855.

Bell D. R., Ihinger P. D. and Rossman G. R. (1995) Quantitative analysis of trace OH in garnet and pyroxenes. *Amer. Miner.* **80**, 465–474.

Beran A. (1976) Messung des Ultrarot-Pleochroismus von Mineralen. XIV. Der Pleochroismus der OH-Streckfrequenz in Diopsid. *Tsch. Miner. Pet. Mitt.* **23**, 79–85.

Brey G. and Köhler T. (1990) Geothermobarometry in four-phase lherzolites II. New thermobarometers, and practical assessment of existing thermobarometers. *J. Petrol* **31**, 1353–1378.

Carpenter S. J. (2003) *The kinetics of hydrogen diffusion in single crystal orthopyroxene* Ph. D. thesis. Penn State Univ.

Carslaw H.S. and Jaeger J.C. (1959) Conduction of heat in solids. Oxford: Clarendon Press, 1959, 2nd ed.

Cheng L., Costa F. and Bergantz G. (2020) Linking fluid dynamics and olivine crystal scale zoning during simulated magma intrusion. *Contrib. Mineral Petrol.* **175**, 53.

Crank J. (1979) *The mathematics of diffusion*. Oxford University Press.

De Hoog J. C. M., Gall L. and Cornell D. H. (2010) Trace-element geochemistry of mantle olivine and application to mantle petrogenesis and geothermobarometry. *Chem. Geol.* **270**, 196–215.

Demouchy S. and Bolfan-Casanova N. (2016) Distribution and transport of hydrogen in the lithospheric mantle: A review. *Lithos* **240–243**, 402–425.

Demouchy S. and Mackwell S. (2003) Water diffusion in synthetic iron-free forsterite. *Phys. Chem. Miner.* **30**, 486–494.

Demouchy S., Jacobsen S. D., Gaillard F. and Stern C. R. (2006) Rapid magma ascent recorded by water diffusion profiles in mantle olivine. *Geology* **34**, 429–432.

Denis C. M. M., Demouchy S. and Shaw C. S. J. (2013) Evidence of dehydration in peridotites from Eifel Volcanic Field and estimates of the rate of magma ascent. *J. Volcanol Geotherm. Res.* **258**, 85–99.

Denis C. M., Alard O. and Demouchy S. (2015) Water content and hydrogen behaviour during metasomatism in the uppermost mantle beneath Ray Pic volcano (Massif Central, France). *Lithos* **236**, 256–274.

Denis C. M. M., Demouchy S. and Alard O. (2018) Heterogeneous hydrogen distribution in orthopyroxene from veined mantle peridotite (San Carlos, Arizona): Impact of melt-rock interactions. *Lithos* **302–303**, 298–311.

Dohmen R. and Chakraborty S. (2007) Fe–Mg diffusion in olivine II: point defect chemistry, change of diffusion mechanisms and a model for calculation of diffusion coefficients in natural olivine. *Phys. Chem. Miner.* **34**, 597–598.

Dohmen R., Becker H.-W. and Chakraborty S. (2007) Fe–Mg diffusion in olivine I: experimental determination between 700 and 1,200°C as a function of composition, crystal orientation and oxygen fugacity. *Phys. Chem. Miner.* **34**, 389–407.

Du Frane W. L. and Tyburczy J. A. (2012) Deuterium-hydrogen exchange in olivine: Implications for point defects and electrical conductivity. *Geochem. Geophys. Geosys.* **13**.

Edmonds M., Kohn S., Hauri E., Humphreys M. and Cassidy M. (2016) Extensive, water-rich magma reservoir beneath southern Montserrat. *Lithos* **252**, 216–233.

Ferriss E., Plank T. and Walker D. (2016) Site-specific hydrogen diffusion rates during clinopyroxene dehydration. *Contrib. Mineral Petrol.* **171**.

Frey F. A. and Prinz M. (1978) Ultramafic inclusions from San Carlos, Arizona: petrologic and geochemical data bearing on their petrogenesis. *Earth Planet Sci. Lett.* **38**, 129–176.

Frost D. J. and McCammon C. A. (2008) The redox state of Earth's mantle. *Annu. Rev. Earth Planet. Sci.* **36**, 389–420.

Gordeychik B., Churikova T., Kronz A., Sundermeyer C., Simakin A. and Wörner G. (2018) Growth of, and diffusion in, olivine in ultra-fast ascending basalt magmas from Shiveluch volcano. *Sci. Rep.* **8**, 1–15.

Gose J., Schmädicke E. and Beran A. (2009) Water in enstatite from Mid-Atlantic Ridge peridotite: Evidence for the water content of suboceanic mantle? *Geology* **37**, 543–546.

Green D. and Ringwood A. (1967) The stability fields of aluminous pyroxene peridotite and garnet peridotite and their relevance in upper mantle structure. *Earth Planet Sci. Lett.* **3**, 151–160.

Hirth G. and Kohlstedt D. L. (1996) Water in the oceanic upper mantle: implications for rheology, melt extraction and the evolution of the lithosphere. *Earth Planet Sci. Lett.* **144**, 93–108.

Ingrin J. and Skogby H. (2000) Hydrogen in nominally anhydrous upper-mantle minerals: concentration levels and implications. *Eur. J. Mineral* **12**, 543–570.

Ingrin J., Latrous K., Doukhan J.-C. and Doukhan N. (1989) Water in diopside: an electron microscopy and infrared spectroscopy study. *Eur. J. Mineral* **1**(3), 327–342.

Jackson A., Parker R. L., Sambridge M., Constable C. and Wolf A. S. (2018) The inverse problem of unpolarized infrared spectroscopy of geological materials: Estimation from noisy random sampling of a quadratic form. *Amer. Miner.* **103**, 1176–1184.

Jochum K. P., Weis U., Stoll B., Kuzmin D., Yang Q., Raczek I., Jacob D. E., Stracke A., Birbaum K. and Frick D. A. (2011) Determination of reference values for NIST SRM 610–617 glasses following ISO guidelines. *Geostand. Geoanal. Res.* **35**, 397–429.

Jollands M. C., Kempf E., Hermann J. and Müntener O. (2019) Coupled inter-site reaction and diffusion: Rapid dehydrogenation of silicon vacancies in natural olivine. *Geochim. Cosmochim. Acta* **262**, 220–242.

Jung H., Katayama I., Jiang Z., Hiraga T. and Karato S.-I. (2006) Effect of water and stress on the lattice-preferred orientation of olivine. *Tectonophysics* **421**, 1–22.

Karato S.-I. (1990) The role of hydrogen in the electrical conductivity of the upper mantle. *Nature* **347**, 272.

Karato S.-I. and Jung H. (2003) Effects of pressure on high-temperature dislocation creep in olivine. *Philos. Mag. (Abingdon)* **83**(3), 401–414.

Kavner A. (2003) Elasticity and strength of hydrous ringwoodite at high pressure. *Earth Planet Sci. Lett.* **214**, 645–654.

Kohlstedt D. L. (2006) The role of water in high-temperature rock deformation. *Rev. Mineral Geochem.* **62**, 377–396.

Kohlstedt D. L. and Mackwell S. J. (1998) Diffusion of hydrogen and intrinsic point defects in olivine. *Z. Phys. Chem. (N.F.)* **207**, 147–162.

Kohn S., Roome B., Smith M. and Howes A. (2005) Testing a potential mantle geohygrometer; the effect of dissolved water on the intracrystalline partitioning of Al in orthopyroxene. *Earth Planet Sci. Lett.* **238**, 342–350.

Kovács I., Hermann J., O'Neill H. S. C., Gerald J. F., Sambridge M. and Horvath G. (2008) Quantitative absorbance spectroscopy with unpolarized light: Part II. Experimental evaluation and development of a protocol for quantitative analysis of mineral IR spectra. *Amer. Miner.* **93**, 765–778.

Lloyd A. S., Ferriss E., Ruprecht P., Hauri E. H., Jicha B. R. and Plank T. (2016) An assessment of clinopyroxene as a recorder of magmatic water and magma ascent rate. *J. Petrol* **57**, 1865–1886.

Lynn K.J. and Warren J.M. (2020) The potential for aqueous fluid-rock and silicate melt-rock interactions to re-equilibrate hydrogen in peridotite nominally anhydrous minerals. Amer. Miner.

Mackwell S. J. and Kohlstedt D. L. (1990) Diffusion of hydrogen in olivine: implications for water in the mantle. *J. Geophys. Res. Solid Earth* **95**, 5079–5088.

Mackwell S., Kohlstedt D. and Paterson M. (1985) The role of water in the deformation of olivine single crystals. *J. Geophys. Res. Solid Earth* **90**, 11319–11333.

Malisa E. and Muhongo S. (1990) Tectonic setting of gemstone mineralization in the Proterozoic metamorphic terrane of the Mozambique Belt in Tanzania. *Precambrian Res.* **46**, 167–176.

Manthilake M., Miyajima N., Heidelbach F., Soustelle V. and Frost D. (2013) The effect of aluminum and water on the development of deformation fabrics of orthopyroxene. *Contrib. Mineral Petrol.* **165**, 495–505.

McDonough W. S. (1990) Constraints on the composition of the continental lithospheric mantle. *Earth Planet Sci. Lett.* **101**, 1–18.

Mutch E. J., Maclennan J., Shorttle O., Edmonds M. and Rudge J. F. (2019) Rapid transcrustal magma movement under Iceland. *Nat. Geosci.* **12**, 569–574.

Nazzareni S., Barbarossa V., Skogby H., Zanon V. and Petrelli M. (2020) Magma water content of Pico Volcano (Azores Islands, Portugal): a clinopyroxene perspective. *Contrib. Mineral Petrol.* **175**, 1–16.

Nekvasil H., Dondolini A., Horn J., Filiberto J., Long H. and Lindsley D. H. (2004) The origin and evolution of silica-saturated alkalic suites: an experimental study. *J. Petrol* **45**(4), 693–721.

Oeser M., Dohmen R., Horn I., Schuth S. and Weyer S. (2015) Processes and time scales of magmatic evolution as revealed by Fe–Mg chemical and isotopic zoning in natural olivines. *Geochim. Cosmochim. Acta* **154**, 130–150.

Padrón-Navarta J. A., Hermann J. and O'Neill H. S. C. (2014) Site-specific hydrogen diffusion rates in forsterite. *Earth Planet Sci. Lett.* **392**, 100–112.

Peslier A. H. (2010) A review of water contents of nominally anhydrous natural minerals in the mantles of Earth, Mars and the Moon. *J. Volcanol Geotherm. Res.* **197**, 239–258.

Peslier A. H., Luhr J. F. and Post J. (2002) Low water contents in pyroxenes from spinel-peridotites of the oxidized, sub-arc mantle wedge. *Earth Planet Sci. Lett.* **201**, 69–86.

Peslier A. H., Schönbächler M., Busemann H. and Karato S.-I. (2017) Water in the Earth's Interior: Distribution and Origin. *Space Sci. Rev.* **212**, 743–810.

Prechtel F. and Stalder R. (2012) OH-defects in Al- and Cr- doped synthetic enstatites and defect geobarometry on natural orthopyroxenes from the Earth's mantle. *Eur. J. Mineral* **24**, 471–481.

Pirzer M. and Sawatzki J. (2008) Method and device for correcting a spectrum. *Patent US7359815B2.*.

Rauch M. and Keppler H. (2002) Water solubility in orthopyroxene. *Contrib. Mineral Petrol.* **143**, 525–536.

Reynes J., Jollands M., Hermann J. and Ireland T. (2018) Experimental constraints on hydrogen diffusion in garnet. *Contrib. Mineral Petrol.* **173**, 69.

Sambridge M., Fitzgerald J., Kovács I., O'Neill H. S. C. and Hermann J. (2008) Quantitative absorbance spectroscopy with unpolarized light: Part I. Physical and mathematical development. *Amer. Miner.* **93**, 751–764.

Sarafian E., Gaetani G. A., Hauri E. H. and Sarafian A. R. (2017) Experimental constraints on the damp peridotite solidus and oceanic mantle potential temperature. *Science* **355**, 942–945.

Satsukawa T., Godard M., Demouchy S., Michibayashi K. and Ildefonse B. (2017) Chemical interactions in the subduction factory: New insights from an in situ trace element and hydrogen study of the Ichinomegata and Oki-Dogo mantle xenoliths (Japan). *Geochim. Cosmochim. Acta* **208**, 234–267.

Schlechter E. (2011) *Electrical conductivity and hydrogen diffusion in synthetic orthopyroxene single-crystals* Ph. D. thesis. Niedersächsische Staats-und Universitätsbibliothek Göttingen.

Schlechter E., Stalder R. and Behrens H. (2012) Electrical conductivity of H-bearing orthopyroxene single crystals measured with impedance spectroscopy. *Phys. Chem. Miner.* **39**, 531–541.

Schmädicke E., Gose J. and Stalder R. (2018) Water in abyssal peridotite: Why are melt-depleted rocks so water rich?. *Geochem. Geophys. Geosyst.* **19**, 1824–1843.

Selway K., Yi J. and Karato S.-I. (2014) Water content of the Tanzanian lithosphere from magnetotelluric data: Implications for cratonic growth and stability. *Earth Planet Sci. Lett.* **388**, 175–186.

Sezerer-Kuru G. and Vural A. (2015) Kilosa-Mwapwa Gold-bearing copper deposits in Tanzania, 68th Geological Congress of Turkey, Ankara

Shea T., Costa F., Krimer D. and Hammer J. E. (2015a) Accuracy of timescales retrieved from diffusion modeling in olivine: A 3D perspective. *Amer. Miner.* **100**, 2026–2042.

Shea T., Lynn K. J. and Garcia M. O. (2015b) Cracking the olivine zoning code: Distinguishing between crystal growth and diffusion. *Geology* **43**, 935–938.

Sio C. K. I., Dauphas N., Teng F.-Z., Chaussidon M., Helz R. T. and Roskosz M. (2013) Discerning crystal growth from diffusion profiles in zoned olivine by in situ Mg–Fe isotopic analyses. *Geochim. Cosmochim. Acta* **123**, 302–321.

Spandler C. and O'Neill H. S. C. (2010) Diffusion and partition coefficients of minor and trace elements in San Carlos olivine at 1,300°C with some geochemical implications. *Contrib. Mineral Petrol.* **159**, 791–818.

Stalder R. (2004) Influence of Fe, Cr and Al on hydrogen incorporation in orthopyroxene. *Eur. J. Mineral* **16**, 703–711.

Stalder R. and Behrens H. (2006) D/H exchange in pure and Cr-doped enstatite: implications for hydrogen diffusivity. *Phys. Chem. Miner.* **33**, 601–611.

Stalder R. and Skogby H. (2003) Hydrogen diffusion in natural and synthetic orthopyroxene. *Phys. Chem. Miner.* **30**, 12–19.

Stalder R. and Skogby H. (2007) Dehydration mechanisms in synthetic Fe-bearing enstatite. *Eur. J. Mineral* **19**, 201–216.

Stalder R., Klemme S., Ludwig T. and Skogby H. (2005) Hydrogen incorporation in orthopyroxene: interaction of different trivalent cations. *Contrib. Mineral Petrol.* **150**, 473–485.

Stalder R., Purwin H. and Skogby H. (2007) Influence of Fe on hydrogen diffusivity in orthopyroxene. *Eur. J. Mineral* **19**, 899–904.

Stalder R., Karimova A. and Konzett J. (2015) OH-defects in multiple-doped orthoenstatite at 4–8 GPa: filling the gap between pure and natural systems. *Contrib. Mineral Petrol.* **169**, 38.

Sundvall R. and Skogby H. (2011) Hydrogen defect saturation in natural pyroxene. *Phys. Chem. Miner.* **38**, 335–344.

Thoraval C. and Demouchy S. (2014) Numerical models of ionic diffusion in one and three dimensions: application to dehydration of mantle olivine. *Phys. Chem. Miner.* **41**, 709–723.

Tian Z.-Z., Liu J., Xia Q.-K., Ingrin J., Hao Y.-T. and Christophe D. (2017) Water concentration profiles in natural mantle orthopyroxenes: A geochronometer for long annealing of xenoliths within magma. *Geology* **45**, 87–90.

Tollan P. and Hermann J. (2019) Arc magmas oxidized by water dissociation and hydrogen incorporation in orthopyroxene. *Nat. Geosci.* **12**, 667–671.

Tollan P. M. E., O'Neill H. S. C., Hermann J., Benedictus A. and Arculus R. (2015) Frozen melt–rock reaction in a peridotite xenolith from sub-arc mantle recorded by diffusion of trace elements and water in olivine. *Earth Planet Sci. Lett.* **422**, 169–181.

Turner M., Turner S., Mironov N., Portnyagin M. and Hoernle K. (2017) Can magmatic water contents be estimated from clinopyroxene phenocrysts in some lavas? A case study with implications for the origin of the Azores Islands. *Chem. Geol.* **466**, 436–445.

Wade J. A., Plank T., Hauri E. H., Kelley K. A., Roggensack K. and Zimmer M. (2008) Prediction of magmatic water contents via measurement of H_2O in clinopyroxene phenocrysts. *Geology* **36**, 799–802.

Wang Y.-F., Qin J.-Y., Soustelle V., Zhang J.-F. and Xu H.-J. (2021) Pyroxene does not always preserve its source hydrogen concentration: Clues from some peridotite xenoliths. *Geochim. Cosmochim. Acta* **292**, 382–408.

Warren J. M. and Hauri E. H. (2014) Pyroxenes as tracers of mantle water variations. *J. Geophys. Res. Solid Earth* **119**, 1851–1881.

Weis F. A., Skogby H., Troll V. R., Deegan F. M. and Dahren B. (2015) Magmatic water contents determined through clinopyroxene: Examples from the Western Canary Islands, Spain. *Geochem. Geophys.* **16**, 2127–2146.

Wilkins R. and Sabine W. (1973) Water content of some nominally anhydrous silicates. *Amer. Miner.* **58**, 508–516.

Woods S. C., Mackwell S. and Dyar D. (2000) Hydrogen in diopside: Diffusion profiles. *Amer. Miner.* **85**, 480–487.

Xia Q.-K., Hao Y., Li P., Deloule E., Coltorti M., Dallai L., Yang X. and Feng M. (2010) Low water content of the Cenozoic lithospheric mantle beneath the eastern part of the North China Craton. *J. Geophys. Res. Solid Earth* **115**, B07207.

Xia Q.-K., Liu J., Kovács I., Hao Y.-T., Li P., Yang X.-Z., Chen H. and Sheng Y.-M. (2019) Water in the upper mantle and deep crust of eastern China: concentration, distribution and implications. *Natl. Sci. Rev.* **6**, 125–144.

Xu Y., Tang W., Hui H., Rudnick R. L., Shang S. and Zhang Z. (2019) Reconciling the discrepancy between the dehydration rates in mantle olivine and pyroxene during xenolith emplacement. *Geochim. Cosmochim. Acta* **267**, 179–195.

Ziberna L., Klemme S. and Nimis P. (2013) Garnet and spinel in fertile and depleted mantle: insights from thermodynamic modelling. *Contrib. Mineral Petrol.* **166**, 411–421.

Associate editor: James Van Orman